Progress In Oceanography
February 2018, Volume 161 Pages 78-86
https://doi.org/10.1016/j.pocean.2018.01.009
https://archimer.ifremer.fr/doc/00629/74109/

Role of the circulation on the anthropogenic CO2 inventory in the North-East Atlantic: A climatological analysis

Carracedo Lidia [1, 2, *], Perez Ff [2], Gilcoto M. [2], Velo A. [2], Padin A. [2], Roson G. [1]

[1] Univ Vigo Spain, Fac Marine Sci, Phys Oceanog Grp GOFUVI, Campus Lagoas Marcosende, Vigo 36200, Spain.
[2] CSIC, Inst Invest Marinas, Oceanol Grp, Eduardo Cabello 6, Vigo 36208, Spain.

* Corresponding author : Lidia Carracedo, email address : lcarracedo@uvigo.es

Abstract :

Climatology-based storage rate of anthropogenic CO2 (C-ant, referred to year 2000) in the North-East Atlantic (53 +/- 9 kmol s(-1), 0.020 +/- 0.003 Pg-C yr(-1)) is described on annual mean terms. C-ant advection (32 +/- 14 kmol s(-1)) occurs mostly in the upper 1800 m and contributes to 60% of the C-ant storage rate. The Azores and Portugal Currents act as 'C-ant streams' importing 389 +/- 90 kmol s(-1), most of which recirculates southwards with the Canary Current (-214 +/- 34 kmol s(-1)). The Azores Counter Current (-79 +/- 36 kmol s(-1)) and the northward-flowing Mediterranean Water advective branch (-31 +/- 12 kmol s(-1)) comprise secondary C-ant export routes. By means of C-ant transport decomposition, we find horizontal circulation to represent 11% of the C-ant storage rate, while overturning circulation is the main driver (48% of the C-ant storage rate). Within the domain of this study, overturning circulation is a key mechanism by which C-ant in the upper layer (0-500 dbar) is drawdown (74 +/- 14 kmol s(-1)) to intermediate levels (500-2000 dbar), and entrained (37 +/- 7 kmol s(-1)) into the Mediterranean Outflow Water to form Mediterranean Water. This newly formed water mass partly exports C-ant to the North Atlantic at a rate of -39 +/- 9 kmol s(-1) and partly contributes to the C-ant storage in the North-East Atlantic (with up to 0.015 +/- 0.006 Pg-C yr(-1)). Closing the C-ant budget, 40% of the C-ant storage in the North-East Atlantic is attributable to anthropogenic CO2 uptake from the atmosphere (21 +/- 10 kmol s(-1)).

Highlights

► North-East Atlantic climatology-based C_{ant} storage rate of 0.020 ± 0.003 Pg-C yr^{-1}. ► C_{ant} import (43 ± 14 kmol s^{-1}) driven by the upper overturning circulation limb. ► Net C_{ant} advection contributes to 60% of the C_{ant} storage rate. ► Atmospheric C_{ant} uptake contributes to 40% of the C_{ant} storage rate. ► 78 ± 30% of the annual air-sea CO_2 uptake is of anthropogenic nature (21 ± 10 kmol s^{-1})

Keywords : Anthropogenic CO2, Carbon storage, Air-sea CO2 uptake, Water masses, Overturning, Gulf of Cadiz, North-East Atlantic

1 Introduction

Human activities such as fossil fuel burning or deforestation have emitted large amounts of CO_2 into the atmosphere (anthropogenic CO_2, C_{ant}) since the Industrial Revolution (1750s), thereby increasing the global atmospheric CO_2 content (Stocker et al., 2013). The ocean plays an important role in the global carbon budget, acting as a net CO_2 sink (Watson et al., 2009). Global model-based studies refer to a mean (2004–2013) CO_2 ocean uptake rate of 2.6 ± 0.5 Pg-C yr^{-1} (Le Quéré et al., 2015). Of the world's oceans, the North Atlantic represents only 13% of the global ocean area, but yet accounts for about one-third of the contemporary global air-to-sea annual CO_2 flux and contains the largest C_{ant} inventory (Sabine et al., 2004). The Atlantic meridional overturning circulation plays a strong part on it by driving the variability of the C_{ant} transport from subtropics to the subpolar North Atlantic (Zunino et al., 2014) and by favoring the CO_2 sink through deep water mass formation (Steinfeldt et al., 2009). Actually, Pérez et al. (2013) suggested that changes in the strength of the overturning circulation in the North Atlantic correlated positively with the C_{ant} storage rate, so the observed reduction of the overturning could be leading to a decrease of CO_2 storage capacity in the subpolar North Atlantic. Therefore, quantifying the transport and storage of C_{ant} in the oceans is relevant for predicting its future evolution in a world of growing CO_2 emissions (Rhein et al., 2013).

More regionally, in the North-East Atlantic (Fig. 1), there is also an overturning cell primarily responsible for the transfer of C_{ant} from surface to deeper levels (Álvarez et al., 2005). In this region, the Strait of Gibraltar yields a unique water mass exchange between salty Mediterranean Outflow Water and East North Atlantic Central Water. The spilling down of Mediterranean Outflow Water towards the Atlantic generates an area of convergence and subduction (overturning circulation) west off the Strait, in the Gulf of Cadiz (Fig. 1). There, central waters are entrained and mixed with Mediterranean Outflow Water to form Mediterranean Water (MW) (van Aken, 2000; Fusco et al., 2008; Carracedo et al., 2016), the salty water mass that ultimately spreads over the entire North Atlantic. Previous studies have focused on the North-East Atlantic as a potential sink for C_{ant} (Ríos et al., 2001; Álvarez et al., 2005; Pérez et al., 2010; Fajar et al., 2012): evaluating the influence of the MW in the CO_2 inventories of the North Atlantic (Álvarez et al., 2005); quantifying the C_{ant} storage in the Gulf of Cadiz (Aït-Ameur and Goyet, 2006; Flecha et al., 2012; Ribas-Ribas et al., 2011); or computing the CO_2 exchange in the Strait of Gibraltar (Huertas et al., 2009).

This paper aims to provide a description of the mean annual climatological C_{ant} transport in the North-East Atlantic across a box defined west of the Gibraltar Strait (Fig. 1), based on GLODAPv2 cruise bottle data (Key et al., 2015; Olsen et al., 2016) and the World Ocean Atlas 2009 climatological database (WOA09, Boyer et al., 2009). We study the contribution of the horizontal and overturning circulation to C_{ant} storage and, as a residual term of the C_{ant} budget, we also provide the anthropogenic contribution to air-sea CO_2 exchange. We first present the data and methods to calculate C_{ant} concentrations (section 2.1), transports (section 2.2) and storage rates in/into/within the box (section 2.3); next, we describe the annual mean C_{ant} spatial distribution (section 3.1) and the part taken by horizontal circulation in C_{ant} redistribution (section 3.2); we then examine and discuss the C_{ant} budget and the main role played by the overturning circulation (section 3.3); and, finally, we present a summary and concluding remarks in section 4.

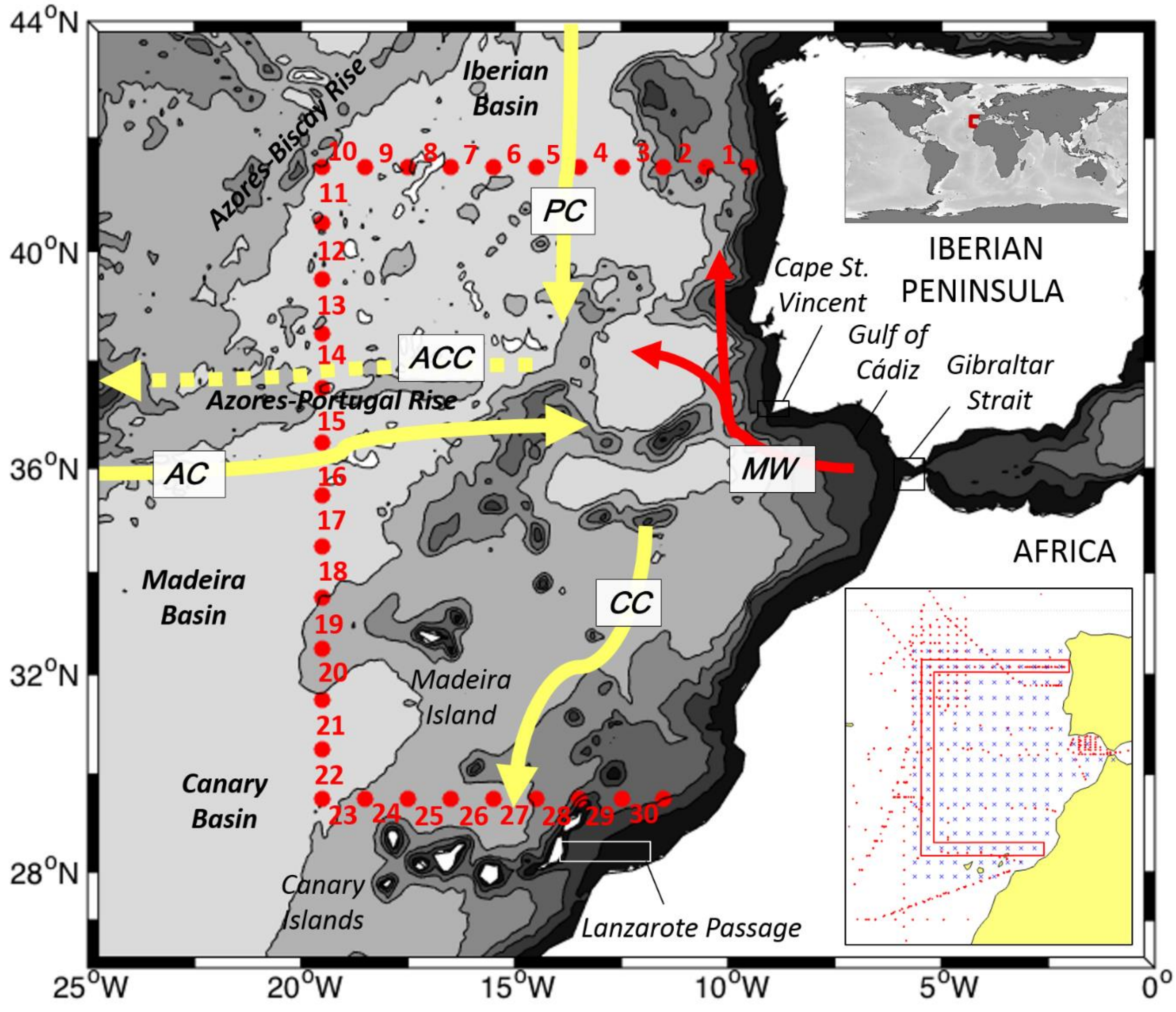

Figure 1. Study area, showing main bathymetric features. Yellow arrows indicate the main surface currents (PC, Portugal Current; AC, Azores Current; CC, Canary Current); yellow dotted arrow

the subsurface Azores Counter Current (ACC); and red arrows the main spreading paths for Mediterranean Water (MW). Red dots mark WOA09-Box station-like positions and red numbers 1 to 30 the station pairs as used for velocity estimates (see section 2.2 for details). Inset figures: upper panel, world map location; lower panel, GLODAPv2 bottle data (red dots), WOA09 grid (blue crosses) and WOA09-Box section (red polygon).

2 Materials and Methods

2.1 C_{ant} concentration

C_{ant} concentrations were estimated by means of a back-calculation technique, the φC_T method (Vázquez-Rodríguez et al., 2009a, 2009b, 2012) (Appendix A.1), which involves the carbonate system variables (total inorganic carbon, total alkalinity and pH) as input data. In this study, these required data were obtained from the GLODAPv2 ocean bottle database (Key et al., 2015; Olsen et al., 2016). A total of 10023 observations were used (Fig. 1, bottom inset figure, red dots). C_{ant} estimates were scaled from their original cruise year to year 2000, for analogy with the sea-air CO_2 flux climatology of Takahashi et al. (2009) (see section 2.4), using the transient steady state approach (Tanhua et al., 2006) (see Appendix A.1).

Once estimated, C_{ant} values were interpolated to the 5574 nodes of the 1ºx1ºx33 levels WOA09 grid resolution of the World Ocean Atlas 2009 (WOA09) database (Boyer et al., 2009) (Fig. 1, bottom inset figure, blue crosses). The interpolation was done using a WMP (Water Masses Properties) multi-parametric interpolation method (Velo et al., 2010) based on WOA09 physical (potential temperature θ, and salinity S) and biogeochemical tracers ("NO" and "PO", where NO = 9 * nitrate + oxygen, PO = 135 * phosphate + oxygen (Anderson and Sarmiento, 1994; Broecker, 1974; Takahashi et al., 1985)). The WMP method consists in an inverse distance weighting algorithm in which the distance is taken in the multi-parametric space from each WOA09 node. Those C_{ant} (ref. 2000) samples with higher associated multi-parametric distance are down-weighted while those closer to the climatologic mean WOA09 nodes are up-weighted. Therefore, the method pushes the final C_{ant} interpolation to a solution closer to the WOA09 climatologic mean, somehow reducing the time discrepancies present on the GLODAPv2 ancillary parameters.

Next, 31 adjacent WOA09 grid nodes were selected as hydrographic "stations" (vertical profiles) so that they formed an enclosed box west of the Gibraltar Strait, as in Carracedo et al. (2014) (referred to as the WOA09-Box hereafter) (Fig. 1). This box was approximately coincident with the 2009 CAIBEX (Shelf–Ocean Exchanges in the Canaries-Iberian Large Marine Ecosystem Project) cruise track (CAIBOX-2009) (Carracedo et al., 2015; Fajar et al., 2012; Lønborg and Álvarez-Salgado, 2014). In Fig. 2b, C_{ant} concentrations for the WOA09-Box limits are shown. For further illustration, spatial distributions of the C_{ant} averaged concentrations (anomalies) at three different depth ranges (0-150, 150-800 and 800-1200 m) are shown in Appendix B (Fig. B1).

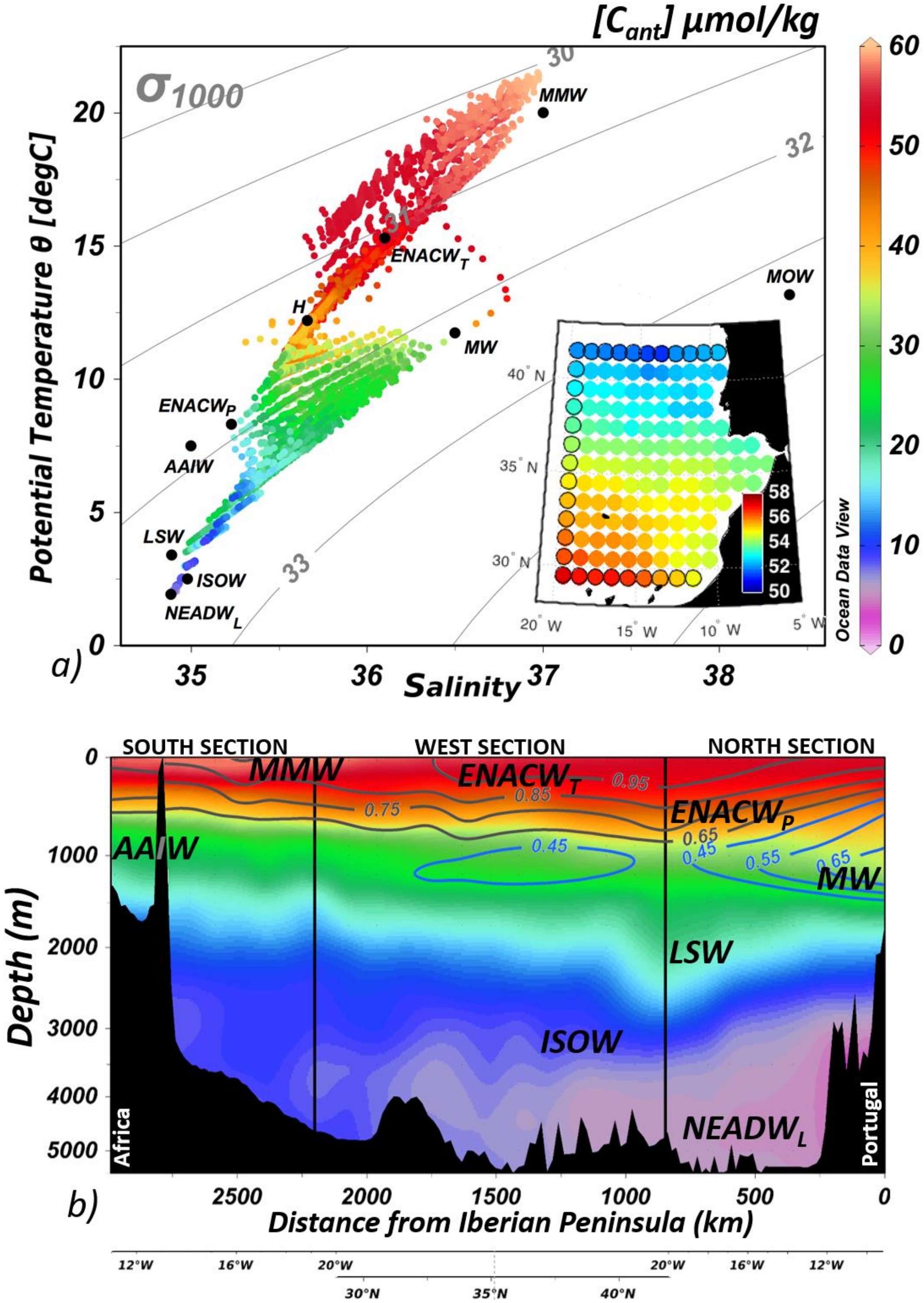

Figure 2. *a)* θ/S diagram of the surface-to-bottom WOA09-Box enclosed data. Color scale represents the concentration of anthropogenic CO_2 (C_{ant}, in μmol kg^{-1}). Black dots denote the source water types of the main water masses present in the region: MMW, Madeira Mode Water; $ENACW_T$, Subtropical East North Atlantic Central Water; $ENACW_P$, Subpolar East North

Atlantic Central Water; MW, Mediterranean Water; MOW, Mediterranean Outflow Water; AAIW, Antarctic Intermediate Water; LSW, Labrador Sea Water; ISOW, Iceland–Scotland Overflow Water; $NEADW_L$, Lower North-East Atlantic Deep Water. Inset figure: horizontal distribution of C_{ant} (μmol kg^{-1}) averaged in the first 150 m of the water column. *b)* Vertical distribution of C_{ant} (μmol kg^{-1}) along the South-West-North limits of the WOA09-Box (section distance refers to accumulated distance from Portugal to Africa). Note color scale is the same as for Fig. 1a.Dark grey isolines correspond to central waters ($MMW+ENACW_T+ENACW_P$) contribution (per one percentage). Dark blue isolines refer to MW contribution (per one percentage).

2.2 C_{ant} transports

The transport of C_{ant} perpendicular to the WOA09-Box, TC_{ant}, is computed as:

$$TC_{ant} = \sum_{j=stp1}^{stp2} \Delta x_j \int_{z1}^{z2} \rho_j \, C_{ant\,j} \, v_j \, dz, \quad (1)$$

For each station pair *j*, ρ_j is seawater density profile (kg m^{-3}), $C_{ant\,j} = C_{ant\,j}(z)$ is the C_{ant} concentration profile (μmol kg^{-1}) and $v_j = v_j(z)$ is the (absolute) velocity profile (m s^{-1}). Δx is the horizontal coordinate (station pair spacing along the perimeter of the WOA-Box, in m), with stp_1 and stp_2 referring to two different station pairs. Station pair notation refers to the mid-point between the 31 WOA09 nodes. *z* is the vertical coordinate (depth, in m), with z_1 and z_2 referring to two different depths. For the C_{ant} transport across the limits of the whole domain (stp_1=1, stp_2=30, z_1=surface, z_2=bottom), we will refer to $T_{Box}C_{ant}$. Note equation (1) expresses the horizontal summation of transports per station pair integrated in depth (1-m resolution profiles). For the across-section absolute velocity field, *v*, we used the estimate by Carracedo et al. (2014), solved by means of a two-dimensional geostrophic inverse ocean model (Mercier, 1986). Briefly, the inverse box model was applied to the three oceanic transects selected from the annual WOA09 dataset. The model, which includes the surface Ekman transport, solves for the reference-level velocities that best satisfy the conservation of volume, salt and heat (and/or other *a priori* specified constraints). Afterwards, the absolute velocity field is computed as the sum of that estimation of velocities at the reference level, and the relative velocities calculated from the density field (i.e., geostrophic velocities obtained by the thermal wind equations). For further details about the method used to compute the absolute volume transports and description of the large-scale gyre circulation in the North-East Atlantic region (Azores Current; Azores Counter Current; Canary Current; Portugal Current; and Iberian Poleward Current), we refer the reader to Carracedo et al. (2014). Hereafter, positive (negative) transports indicate flows into (out of) the box.

Finally, to further assess the elements of the circulation that influence the advection of C_{ant}, TC_{ant} was decomposed into three components (Álvarez et al., 2005): a throughflow or barotropic term due to the net transport across the box and the section-averaged C_{ant} ($T_{baro}C_{ant}$); a baroclinic or overturning term due to the horizontally averaged vertical structure of the velocity and C_{ant} fields ($T_{over}C_{ant}$); and finally, a horizontal term due to the residual velocities and residual C_{ant} concentrations after the barotropic and overturning components have been subtracted that is associated with the gyre circulation ($T_{horiz}C_{ant}$). According to that, TC_{ant} was split as:

$$TC_{ant} = T_{baro}C_{ant} + T_{over}C_{ant} + T_{horiz}C_{ant}$$

$$TC_{ant} = \rho \, \langle C_{ant} \rangle \, V_0 \int L(z)\, dz + \rho \int \langle C_{ant} \rangle(z) \langle v \rangle(z) \, L(z)\, dz + \rho \sum_{j=stp1}^{stp2} \Delta x_j \int C_{ant\,j}{}'(z)\, v_j{}'(z)\, L_j(z)\, dz \qquad (2)$$

where ρ refers to the mean seawater density, V_0 is the section-averaged velocity ($V_0 = T_{Box}/A$, with T_{Box} being the net volume transport across the section, i.e., the North, West and south bounds of the box, and A the total area of the section). $<v>(z)$ is the mean vertical profile of the velocity anomalies ($v(x,z)$ - V_0). $v_j'(z)$ represents the deviations from the mean vertical profile ($v_j'(z) = v_j(z) - <v>(z)$). For C_{ant}, $<C_{ant}>$ represents the section mean, $<C_{ant}>(z)$ is the mean vertical profile of C_{ant} anomalies ($C_{ant}(x,z) - <C_{ant}>$), and $C_{ant\,j}'(z)$ are the deviations from the corresponding mean vertical profile ($C_{ant\,j}'(z) = C_{ant\,j}(z) - <C_{ant}>(z)$).

In order to evaluate the contribution of central waters and MW to the C_{ant} budget, we used the water mass fractions solved by Carracedo et al. (2014), by means an Optimum MultiParameter mixing analysis (OMP analysis, Tomczak, 1981; Pardo et al., 2012). $c_{wm\,j} = c_{wm\,j}(z)$ is the water mass contribution profile with values in the range 0–1, that reflects the proportion of a given water mass involved in the mixing process (0 indicates no contribution and 1 100% contribution). By combining C_{ant} transports with water mass fractions, we can estimate the relative contribution of each water mass as follows:

$$(TC_{ant})_{wm} = \sum_{j=stp1}^{stp2} \Delta x_j \int_{z1}^{z2} \rho_j \; C_{ant_j} \; v_j \; c_{wm_j} \; dz \qquad (3)$$

Likewise, to determine the MW or central waters contribution to the Cant transport decomposition (Eq. 2), each component ($T_{net}C_{ant}$, $T_{over}C_{ant}$, $T_{horiz}C_{ant}$) was multiplied by the respective contribution matrix (c_{MW}, for MW; or c_{CW}, for central waters). Central waters and MW contribution are shown in Fig. 2b. Note in this study, central waters account for the sum contribution of three end-members, as solved by Carracedo et al. (2014): the Madeira Mode Water (MMW) and the Subtropical and Subpolar East North Atlantic Central Water ($ENACW_T$ and $ENACW_P$, respectively) (Fig. 2a, Table A2).

2.3 Calculation of C_{ant} budget

In order to study the C_{ant} budget in the region, the inventory of C_{ant} (*C_{ant} inventory*) was computed by integrating C_{ant} concentrations vertically and horizontally, considering all WOA09 nodes inside the box (Fig. 1, inset figure):

$$C_{ant}\ inventory = \iiint C_{ant}\, dx\, dy\, dz \qquad (4)$$

C_{ant} inventory can be given as a total inventory, in Pg-C (1 Pg-C=1 GtC), or, alternatively, as specific inventory (per unit area), in molC m^{-2}. Provided the transient steady state assumption (Tanhua et al., 2006; Keeling and Bolin, 2010), the time derivative of C_{ant} (*C_{ant} storage rate*) can be obtained by multiplying the *C_{ant} inventory* by the annual C_{ant} rate of increase k_t ($k_t = 0.0169 \pm 0.0010\ y^{-1}$, Steinfeldt et al. (2009)) Therefore,

$$C_{ant}\ storage\ rate = k_t\, C_{ant}\ inventory \qquad (5)$$

The transient steady state assumption implies that through the whole water column, C_{ant} will increase over time at a rate that is proportional to the C_{ant} increase in the mixed layer. In a recent study carried out in the Equatorial Atlantic Ocean, Fajar et al. (2015) found that the estimated C_{ant} storage rates were consistent, within the uncertainties, to those based on the steady state assumption. This supports the feasibility of using this premise in a climatological data-based framework. As for the *C_{ant} inventory*, note the *C_{ant} storage rate* can also be given as specific storage rate (per unit area), in molC m^{-2} y^{-1}; or as total storage rate, in Pg-C y^{-1} or kmol s^{-1}.

The final C_{ant} budget within any oceanic basin will result from the balance between lateral advection (box across-boundaries' transports), air-sea fluxes and the storage rate in the form:

$$C_{ant}\ storage\ rate = T_{Box}C_{ant} + T_{Strait}C_{ant} + F_{Air\text{-}sea}C_{ant} \qquad (6)$$

where *C_{ant} storage rate* is estimated with Eq. (5). $T_{Box}C_{ant}$ refers to the net transport of C_{ant} across the northern, western and southern limits of WOA09-Box, as estimated from Eq. (1). $T_{Strait}C_{ant}$ refers to the net transport of C_{ant} across the Strait of Gibraltar. For $T_{Strait}C_{ant}$, we used the estimate of Huertas et al. (2009), who calculated a 2-year mean net flux of C_{ant} towards the Mediterranean basin of 4.20 ± 0.04 Tg C yr^{-1}, that is, 11 ± 1 kmol s^{-1}. This value is in agreement with Álvarez et al. (2005). Note that according to our sign convention (fluxes out of WOA09-Box take a negative sign) $T_{Strait}C_{ant}$ becomes -11 ± 1 kmol s^{-1}. Finally, $F_{Air\text{-}sea}C_{ant}$ refers to the net air-sea anthropogenic CO_2 flux in the region. Among the four terms of the equation, $F_{Air\text{-}sea}C_{ant}$ is the one introducing a higher uncertainty to the budget estimate, so that this term was isolated from Eq. (6), considered an unknown and, therefore, became our final target.

2.4 Air-sea CO_2 exchange

In order to assess the C_{ant} budget depicted by our results, the $F_{Air\text{-}sea}C_{ant}$ estimate (Eq. 6) was compared to the total air-sea CO_2 exchange in the region ($F_{Air\text{-}sea}\ CO_2$). The annual average of the monthly air-sea CO_2 fluxes was obtained from the global climatology of Takahashi et al. (2009). Their monthly $F_{Air\text{-}sea}\ CO_2$ estimate is the product of the sea–air pCO_2 difference (ΔpCO_2, in µatm; see Fig. B2 in Appendix B) and the air–sea gas transfer rate (*Tr*, in kmol m^{-2} $month^{-1}$ μatm^{-1}), both referenced to year 2000. For more details about the source datasets required for the monthly climatologic air-sea CO_2 flux calculation and/or for *Tr* formulation, the reader is referred to Takahashi et al. (2009). From their original spatial resolution of 4º (latitude) × 5º (longitude), we spatially interpolated the data to the WOA09 grid. Finally, we averaged the flux estimates considering the whole WOA09-Box surface (1.36×10^{12} m^2) so that obtaining the annual mean air-sea CO_2 exchange within our domain of study.

3 Results and Discussion

3.1 C_{ant} distribution

The C_{ant} distribution shows the characteristic vertical decreasing gradient in depth (Fig. 2b). Maximum concentrations of C_{ant} (~60 µmol kg^{-1}) are found in the first 150 m of the water column, where the highest proportion of East North Atlantic Central Water is present (Carracedo et al., 2014). Within this layer, the horizontal C_{ant} distribution (Fig. 2a, inset figure) shows a marked latitudinal gradient, with increasing concentration towards the equator. Lower C_{ant} values off the

African coast are due to the year-round upwelling of deep waters with low C_{ant} (Speth et al., 1978). Below the upper layer (>150 m), C_{ant} decreases slowly down to 1200 m (Fig. 2b), with a sharper gradient in the southern side of the box compared to the northern side. That relates to the presence of Antarctic Intermediate Water with lower C_{ant} content (~22 μmol kg $^{-1}$) south of the region, in contrast to the occurrence, further north, of MW with a higher C_{ant} (30-35 μmol kg $^{-1}$). The relative maximum at the 2000-m level (~20 μmol kg $^{-1}$) is linked to the Labrador Sea Water entering the box through its north-west corner (Carracedo et al., 2014). At depths bellow 2000m, C_{ant} concentration is low (<15 μmol kg^{-1}) but still noticeable, due to the deep penetration of C_{ant} in the high-latitude regions of the North Atlantic by the formation and subsequent spreading of the North Atlantic Deep Water (Woosley et al., 2016). The lowest C_{ant} values are found in the southern corner of the box, related to the presence of the deepest component of the North-East Atlantic Deep Water, the remains of the southern-ocean origin Antarctic Bottom water (Carracedo et al., 2014).

3.2 Role of the horizontal advection in the C_{ant} distribution

The advective C_{ant} transports across the limits of WOA09-Box are shown in Fig. 3a. We obtained a net flux of **43 ± 14 kmol s^{-1}** ($T_{Box}C_{ant}$, Eq. 1). For a similar box in the same region, but built by combination of three different non-synoptic cruise sections, Álvarez et al. (2005) obtained a net C_{ant} transport of 66 ± 14 kmol s^{-1}. Although being higher the latter, neither value is statistically distinguishable within the uncertainties. It is notable, however, that quasi-synoptic cruise-based tracer transport estimates are affected by mesoscale and seasonal variability and may not necessarily be representative of an annual climatology.

As depicted in Fig. 3a, C_{ant} transport is stronger in the upper 1500 m. In fact, the 0-1500 m depth range accounts for more than 90% of the C_{ant} advection. This underlines the upper/intermediate circulation as responsible for C_{ant} redistribution and transport into/out of the region. By estimating TC_{ant} of the main currents (see integration limits by currents in Table 1), we find that the Canary Current is the main current exporting C_{ant} out of the box (-214 ± 34 kmol s^{-1}), while the Azores Current is the main input source (314 ± 88 kmol s^{-1}). From the total net 389 ± 90 kmol s^{-1} of C_{ant} being imported by Portugal and Azores Currents, around 20% recirculates westwards and northwards, within the Azores Counter Current (-79 ± 36 kmol s^{-1}) and the Iberian Poleward Current (-11 ± 3 kmol s^{-1}), respectively; while more than a half (55%) is transported southwards by the Canary Current.

Table 1. Spatial limits, defining main surface and subsurface currents (as in Carracedo et al., 2014, but here with depth instead of pressure as vertical coordinate, assuming that 1dbar~1m); and their corresponding volume (Sv, Sverdrup [= 10^6 m^3 s^{-1}]) and C_{ant} (kmol s^{-1}) transports. PC, Portugal Current; IPC, Iberian Poleward Current; ACC, Azores Counter Current; AC, Azores Current; CC, Canary Current. T_{sw} refers to sea water volume transport (Sv).

		Spatial limits				***Mean properties***			***C_{ant} transport***
		St. pairs	*Horiz. limits*	*Vert. limits, m*	*Condition*	*θ ºC*	*S psu*	*C_{ant} μmol kg^{-1}*	*TC_{ant}, kmol s^{-1} (Net vol, Sv)*
Currents	*PC*	1 to 11	9.1 to 20^0W	0-800	T_{sw}>0	12.0	35.68	48.0	83.5 ± 12 (1.4 ± 0.4)
	IPC	1 to 2	9.1 to 10.4^0W	0-300	T_{sw} <0 & S≥35.8	14.2	35.84	52.3	-10.6 ± 2 (-0.98 ± 0.3)
	ACC	12 to 18	34 to 40^0N	400-1800	T_{sw} <0	8.4	35.55	27.7	-71.8± 11 (-2.5 ± 0.8)
	AC	15 to 22	30 to 37^0N	0-1600	T_{sw}>0	11.7	35.79	36.9	307.1 ± 24 (6.5 ± 0.8)

CC	19 to 30	20 to 12. 9^0W	0-600	T_{sw} <0	15.2	36.12	48.3	-207.0 ± 13 (-4 ± 0.4)

Moving on to the C_{ant} transport decomposition shown in Eq. (3), the horizontal component ($T_{horiz}C_{ant}$) has a net value of -13 ± 2 kmol s^{-1}, which represents a 11% contribution to the net C_{ant} transport across the limits of WOA09-Box. The origin of its negative sign differs latitudinally. North of 36ºN (north of the Azores Current), the negative sign of the horizontal component comes from the combination of positive C_{ant} anomalies (water masses with higher C_{ant} content than the mean) and a negative net transport, while south of that latitude, the negative sign comes from the combination of negative C_{ant} anomalies (water masses with lower C_{ant} content than the mean) and a positive net transport (Fig. 3b). To locate the main region contributing to $T_{horiz}C_{ant}$, the latter was vertically integrated and horizontally accumulated from the Iberian coast to the African coast (Fig. 3c, black line). Similarly, to locate the depth range contributing the most to $T_{horiz}C_{ant}$, this component of the C_{ant} transport was horizontally integrated and vertically accumulated from surface to bottom (Fig. 4a, dark grey line). The strongest $T_{horiz}C_{ant}$ occurs off the Iberian coast and across the southern section, and mostly between 650 and 1500 m. This means the horizontal C_{ant} transport is driven by the combination of the intermediate circulation and the contrasting C_{ant} content of the water masses at those regions.

To evaluate the role of the central waters and MW on the advection of C_{ant}, we isolated the C_{ant} transport by water masses, as explained in section 2.2. (Eq. 3). Central waters import C_{ant} into the WOA09-Box from the North Atlantic Ocean at a net rate of 89 ± 55 kmol s^{-1} (0.03 ± 0.02 Pg-C yr^{-1}) (Fig. 3d, red line); whereas MW exports C_{ant} from the region of study to the North Atlantic at a net rate of -39 ± 9 kmol s^{-1} (-0.015 ± 0.003 Pg-C yr^{-1}) (Fig. 3d, blue line), most of it northwards (-31 ± 11 kmol s^{-1}; Fig. 3d, red line). These C_{ant} transports are significantly smaller than those obtained by Álvarez et al. (2005) (-88 ± 8 kmol s^{-1} or 0.03 ± 0.003 Pg-C yr^{-1} for MW; 144 ± 8 kmol s^{-1} or 0.055 ± 0.003 Pg-C yr^{-1} for central waters). Focusing just on the horizontal component of the C_{ant} transport ($T_{horiz}C_{ant}$, Eq. 2) by water masses, we find 49% of this component is driven by central waters (Fig. 3c, red line and bars), 45% by MW (Fig. 3c, red line and bars), and the remaining 6% is due to the sum contribution of other water masses (not shown). Therefore, we can point to central waters and MW as the main contributors to the horizontal component of the C_{ant} transport.

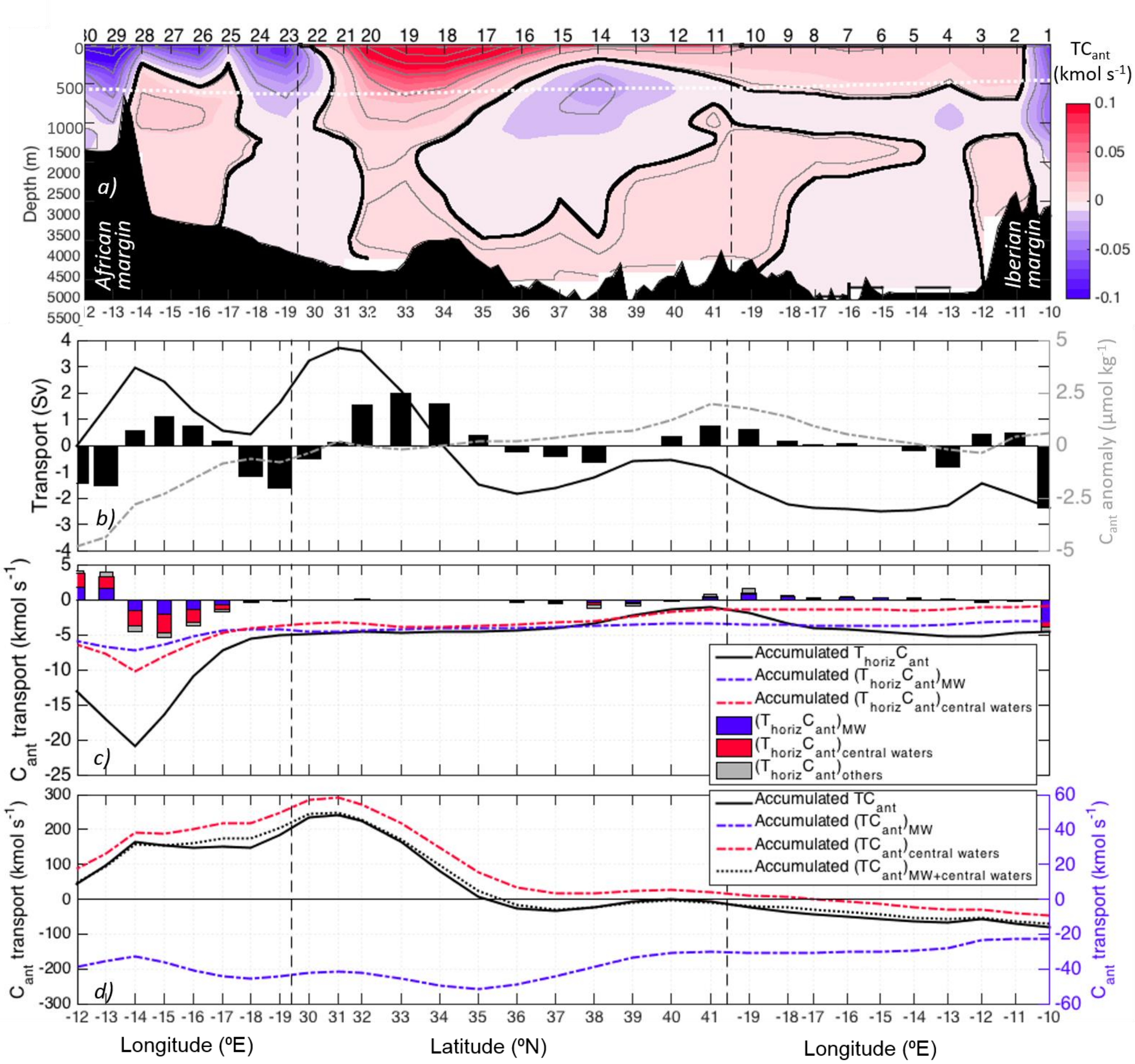

Figure 3. *a)* C_{ant} transports (kmol s^{-1}) orthogonal to the WOA-Box. Grey contours represent mass transport (in Sv) (black bold line is the null transport isoline). Positive (negative) values indicate C_{ant} transports into (out of) the WOA09-Box. The white dotted line corresponds to the isopycnal σ_1 = 31.65 kg m^{-3} (potential density referred to 1000 dbar), which separates the upper and lower limbs of the overturning circulation (Carracedo et al., 2014); *b)* On the left axis: the solid line is the horizontally accumulated (from the Iberian Peninsula to Africa) volume transport (vertically integrated for the whole water column) and the vertical bars indicate the total transport per station pair. On the right axis: the dash-dotted grey line shows the mean value of C_{ant} anomalies (C_{ant}(x, z) - <C_{ant}>, where <C_{ant}> represents the section mean), in µmol kg^{-1}, vertically averaged along the section; *c)* Horizontally accumulated (from the Iberian Peninsula to Africa) horizontal component of the C_{ant} transport (vertically integration for the whole water column) (black line). Mediterranean Water horizontal C_{ant} transport (blue dash-dotted line), and central waters horizontal C_{ant} transport (red dash-dotted line), accumulated from the Iberian to the African coast, are also shown. Vertical bars indicate the net horizontal component of the C_{ant} transport per station pair, with the contribution of Mediterranean (blue) and Central Waters (red) specified; *d)* Horizontally

accumulated (from the Iberian Peninsula to Africa) C_{ant} transport (vertically integrated for the whole water column, black line). Mediterranean Water C_{ant} transport (blue dash-dotted line, right axis), central waters C_{ant} transport (red dash-dotted line, left axis), and the sum of C_{ant} transports of both water masses (dotted line, left axis), all accumulated from the Iberian peninsula to Africa, are also shown.

3.3 Anthropogenic CO_2 inventory and role of the overturning circulation

For the WOA09-Box enclosed region, the C_{ant} *inventory* was computed by vertical integration of the C_{ant} grid data (Eq. 4). We estimated a total inventory of 1.18 ± 0.20 Pg-C, which, considering the total surface area of WOA09-Box (1.36×10^{12} m^2), results in a specific inventory of 72 ± 12 molC m^{-2}. Lee et al. (2003), based on *in situ* data (1990-1998 period), provided an estimate, referenced to 1994, of 66.2 molC m^{-2} for the 30°N–40°N latitudinal band. Similarly, and also based on hydrographic cruise data (1993–2003 period), Vázquez-Rodríguez et al. (2009a) provided a specific C_{ant} *inventory* of around 75 molC m^{-2} (referenced to 1994) at 30°N. When rescaled to year 2000 (reference year in this study) (Eq. A1), both values (73.2 and 82.9 molC m^{-2}, respectively) are comparable to our estimate within the uncertainty. At more regional scale, Flecha et al. (2012) determined a specific C_{ant} *inventory* of 33.5 ± 3.2 molC m^{-2} in the Gulf of Cadiz (Fig. 1, total area of 0.04×10^{12} m^2) from *in situ* cruise data (October 2008). The GLODAPv2-based estimate for that particular region is 40 ± 8 molC m^{-2} (referenced to 2000). To compare both estimates, we rescaled Flecha's et al. (2012) value to year 2000 (Eq. A1), resulting in 29.3 ± 2.8 molC m^{-2}. Although our estimate is slightly larger than that of Flecha's et al. (2012), they are not statistically different. Note the specific C_{ant} *inventory* in the Gulf of Cadiz region is smaller in comparison to the average for the entire WOA09-Box region (see Fig. B3 in Appendix B). That could be interpreted as the Gulf of Cadiz, despite being the location where the exchange of C_{ant} between central and intermediate water masses takes place, is not the region where C_{ant} is stored. Finally, by multiplying the C_{ant} *inventory* by k_t (0.0169 yr^{-1}), we obtained a C_{ant} *storage rate* of **0.020 ± 0.003 Pg-C yr^{-1}** (that is, **53 ± 9 kmol s^{-1}**). That implies a specific C_{ant} *storage rate* of 1.22 ± 0.21 molC m^{-2} y^{-1}. Ríos et al. (2001), who used a set of 12 cruises carried out in the North-East Atlantic between 1977 and 1997, estimated a similar but slightly lower specific storage rate of 0.95 molC m^{-2} y^{-1}. The good overall agreement with *in situ*-based studies in terms of C_{ant} inventory/storage rate adds confidence to our climatology-based estimates.

According to the transport decomposition (Eq. 2), there is a net overturning component, $T_{over}C_{ant}$, of 56 ± 2 kmol s^{-1}. Note the barotropic component ($T_{baro}C_{ant}$= 0.2 ± 8 kmol s^{-1}, Eq. 2) has an almost negligible contribution to the net C_{ant} flux, so we are just discussing horizontal vs. overturning components. By vertical (surface-to-bottom) accumulation of $T_{over}C_{ant}$ (Fig. 4a, light grey line), we see that the upper limb of the overturning circulation (σ_1 < 31.65 kg m^{-3}, Fig. 3a, broadly upper 500 m) is the main driver of the term. That is, the C_{ant}-loaded surface waters (Fig. 2) imported by the upper overturning cell (72 ± 6 kmol s^{-1}) will not be compensated for the less C_{ant}-loaded waters (Fig. 2) exported by the lower limb (-17 ± 9 kmol s^{-1}), thus resulting in a positive $T_{over}C_{ant}$ component (56 ± 2 kmol s^{-1}). This component is four times larger than the horizontal component ($T_{horiz}C_{ant}$, -13 ± 2 kmol s^{-1}), meaning that net C_{ant} transport is mostly driven by overturning circulation (80%) rather than by horizontal circulation (20%). This resembles the larger scale, where the North Atlantic meridional overturning circulation is found to drive both the magnitude and variability of the C_{ant} transport across the Subpolar North Atlantic (Zunino et al., 2014). Our results confirm the cruise-based findings of Alvarez et al. (2005), and let us further denote this physical mechanism as the main driver of the net C_{ant} transport in the North-East Atlantic in the long-term average context of an annual climatology.

As for the overturning circulation within the box, when MW is formed in the Gulf of Cadiz (with an upper bounded MW production rate of 2 Sv, Carracedo et al. 2014, 2015), 1.2 ± 0.2 Sv of central waters are entrained into the sinking plume of Mediterranean Outflow Water (Carracedo et al., 2014; Barbosa Aguiar et al., 2015). Since central waters at this location have a C_{ant} concentration of about 60 ± 6 µmol kg^{-1} (Huertas et al., 2009), this entrainment provides about 74 ± 14 kmol s^{-1} of C_{ant} (0.03 ± 0.01 Pg-C yr^{-1}) to intermediate layers. Prior studies have reported higher amounts of C_{ant} drawdown to depth by central waters (185 kmol s^{-1} or 0.07 Pg-C yr^{-1}, Ríos et al. 2001; 151 ± 14 kmol s^{-1} or 0.06 ± 0.01 Pg-C yr^{-1}, Álvarez et al. 2005). Those studies, however, could have overestimated the volume of central waters (3-4 Sv) being entrained, as shown in the recent study by Barbosa Aguiar et al. (2015). Half of those 74 ± 14 kmol s^{-1}, 37 ± 7 kmol s^{-1} (0.6 ± 0.1 Sv, Carracedo et al. 2014), are finally merged with 0.78 ± 0.05 Sv (Soto-Navarro et al., 2010) of Mediterranean Outflow Water to form MW. Considering a mean C_{ant} concentration of 52 ± 6 µmol kg^{-1} for the Mediterranean Outflow Water (Huertas et al., 2009), this overflow provides an input of 42 ± 5 kmol s^{-1} of C_{ant}. Therefore, the resulting MW is going to contribute with around 79 ± 9 kmol s^{-1} of C_{ant}. According to our results, 39 ± 9 kmol s^{-1} of C_{ant} are (net) exported by MW out of the WOA09-Box, so that the remaining 40 ± 13 kmol s^{-1} (0.015 ± 0.005 Pg-C yr^{-1}) would be available to contribute to the total C_{ant} storage rate within the box (0.020 ± 0.003 Pg-C yr^{-1}).

In the context of the subtropical North Atlantic (total area of 16.6 × 10^{12} m^2), the singular overturning cell that occupies the localized region of the Gulf of Cadiz can be pointed as a relevant conduit through which C_{ant} sinks (0.03 Pg-C yr^{-1}) and ultimately contributes to the storage rate at intermediate layers (0.015 ± 0.005 Pg-C yr^{-1}) within the WOA09-Box. This contribution of the newly formed MW to the storage rate represents a 6% of the total C_{ant} stored in the subtropical North Atlantic (0.280 ± 0.011 Pg-C yr^{-1} referenced to 2004, Pérez et al., 2013; 0.262 ± 0.010 Pg-C yr^{-1} referenced to 2000, Eq. A1), despite the Gulf of Cadiz accounting for less than 1% of the subtropical North Atlantic surface.

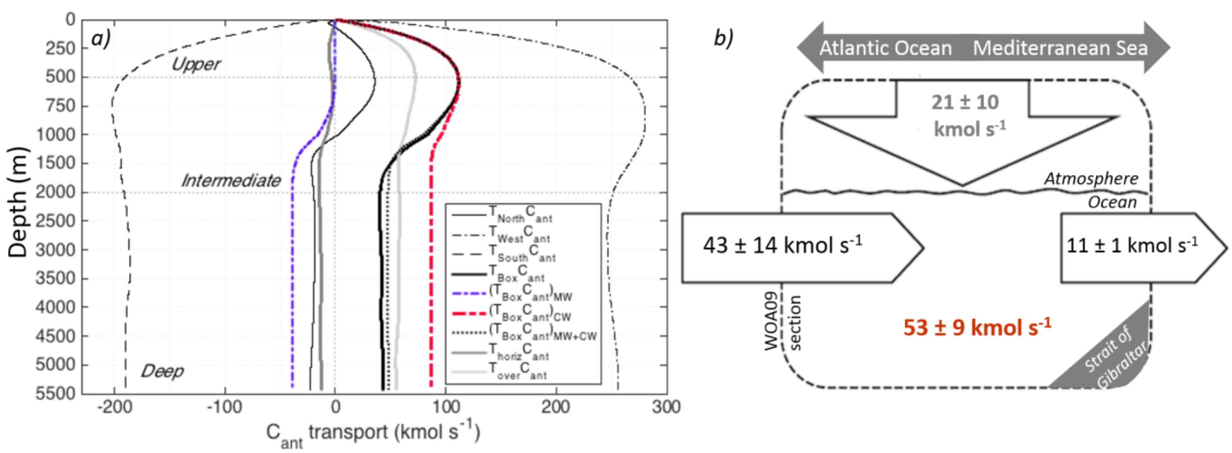

Figure 4. *a)* Vertical distribution of vertically (surface-to-bottom) accumulated C_{ant} transports ($T_{North}C_{ant}$, $T_{West}C_{ant}$, $T_{South}C_{ant}$, refer to the C_{ant} transports across north, west and south sections, respectively; $T_{Box}C_{ant}$, the C_{ant} transport across the whole section; $(T_{Box}C_{ant})_{MW}$, $(T_{Box}C_{ant})_{CW}$ and

$(T_{Box}C_{ant})_{MW+CW}$ refers to the C_{ant} transport by the Mediterranean Water, by central waters, and by the sum of those two water masses, respectively; and $T_{horiz}C_{ant}$ and $T_{over}C_{ant}$ the horizontal and overturning components, transports in kmol s^{-1}; *c)* Simplified C_{ant} budget scheme for WOA09-Box.

Finally, closing the C_{ant} budget in the North-East Atlantic at climatological scale (Fig. 4b), we estimated the anthropogenic air-to-sea contribution for WOA-Box following Eq. (6). The net annual $F_{Air\text{-}sea}C_{ant}$ was **21 ± 10 kmol s^{-1}**, not distinguishable, within the uncertainty, to the value obtained by Álvarez et al. (2005) of 13 kmol s^{-1}. The magnitude of this term (21 ± 10 kmol s^{-1}) represents 40% of the total C_{ant} storage (53 ± 9 kmol s^{-1}), while advection ($T_{Box}C_{ant}$ + $T_{Strait}C_{ant}$ = 32 ± 14 kmol s^{-1}) contributes the remaining 60% to the C_{ant} budget (11% due to the horizontal component and 48% to the overturning component). C_{ant} advection being predominant over air-sea C_{ant} flux is a result in agreement with Álvarez et al. (2005). They concluded that 17% of the C_{ant} storage was attributable to uptake from the atmosphere, compared to 83% coming from the ocean circulation. Ríos et al. (2001), however, had previously estimated that the atmospheric input of C_{ant} (0.47 mol m^{-2} yr^{-1}) contributed as much as advection to the C_{ant} inventory within the Iberian Basin (at 20^{0}W and 37-47^{0}N latitudinal range).

The total (natural and anthropogenic) CO_2 air-sea flux in the region, $F_{Air\text{-}sea}$ CO_2 (section 2.4.), has a magnitude of **27 ± 8 kmol s^{-1}** (annual average of monthly estimates), meaning that on annual timescales the North-East Atlantic acts as a sink for atmospheric CO_2. The anthropogenic portion of the total $F_{Air\text{-}sea}$ CO_2, inferred from our results at the 28-42^{O}N latitudinal range (21 ± 10 kmol s^{-1}), represents more than three quarters of the total CO_2 uptake (78 ± 30%). The difference between both magnitudes, $F_{Air\text{-}sea}$ CO_2 and $F_{Air\text{-}sea}C_{ant}$, is attributable to the natural component ($F_{Air\text{-}sea}C_{nat}$, 6 ± 12 kmol s^{-1}). In the North Atlantic, the air-sea CO_2 fluxes result from anthropogenic forcing and progressive northward cooling of the upper limb of the meridional overturning circulation (Pérez et al., 2013), the latter being ultimately responsible for the North Atlantic uptake of natural CO_2 (Pérez et al., 2013). For a box encompassing the subtropical region (between 25ºN and the A25 section, see their Fig. 1a), Pérez et al. (2013) found the anthropogenic air-sea CO_2 uptake dominated (60 ± 25% of the total air-sea CO_2 flux) over the natural component; whereas for the subpolar region (between the A25 section and the Nordic sills, see their Fig. 1a), the natural component was largely prevalent over the anthropogenic one (which only represented 18 ± 13% of the total air-sea CO_2 flux). The anthropogenic air-sea CO_2 uptake inferred from our estimates within the domain of the WOA09-Box (29.5-41.5ºN latitudinal range) leads us to interpret the region of study as part of the air-sea C_{ant}-dominated subtropical regime, as defined by Pérez et al. (2013). However, because of the large uncertainties accompanying the air-sea fluxes and the indirect nature of the $F_{Air\text{-}sea}C_{ant}$ estimate, our interpretation about C_{nat} *vs.* C_{ant} contribution must be taken with some caution.

4 Summary and concluding remarks

In this study, we presented a description of the mean annual C_{ant} transport in the Azores-Gibraltar region and evaluated the role of the horizontal and overturning circulation in terms of C_{ant} storage in the North-East Atlantic. To the best of our knowledge, C_{ant} budget estimates are given for the first time in this region by combination of C_{ant} GLODAPv2-derived concentrations and WOA09-derived absolute velocity field.

We obtained a net C_{ant} transport across the WOA09-Box section of 43 ± 14 kmol s^{-1}. The 0-1500 m depth range encompasses more than 90% of the C_{ant} advection, underlining the upper/intermediate circulation as responsible for C_{ant} distribution and recirculation within the region. Azores and Portugal Currents account for the greatest C_{ant} inflow, with 389 ± 90 kmol s^{-1}. Most of it recirculates southwards in the Canary Current (-214 ± 34 kmol s^{-1} of C_{ant}), which provides the main advective C_{ant} export path across the limits of WOA09-Box. At intermediate levels, we find the secondary C_{ant} export route to be the Azores Counter Current, with a westwards C_{ant} flux of -79 ± 36 kmol s^{-1}.

At annual mean climatological scale, we estimated a total *C_{ant} inventory* of 1.18 ± 0.20 Pg-C (specific inventory of 72 ± 12 molC m^{-2}) and a *C_{ant} storage rate* of 0.020 ± 0.003 Pg-C yr^{-1} (53 ± 9 kmol s^{-1}). The advection of C_{ant} contributes to 60% of the North-East Atlantic C_{ant} storage rate. Of the 60% contribution, 11% is driven by horizontal circulation (-13 ± 2 kmol-C_{ant} s^{-1}) and 48% is driven by overturning circulation (56 ± 2 kmol-C_{ant} s^{-1}). Overturning circulation is, therefore, the physical mechanism dominating the C_{ant} transport across the limits of WOA09-Box and, ultimately, the C_{ant} storage rate in the North-East Atlantic. The remaining 40% (21 ± 10 kmol s^{-1}) is due to the atmospheric C_{ant} being taken up by the ocean. The anthropogenic fraction of the atmospheric CO_2 accounts for more than three quarters (78 ± 30%) of the total annual air-sea (natural and anthropogenic) CO_2 uptake at a climatological scale in the region (27 ± 8 kmol s^{-1}).

Exploring the water mass transformation as result of the overturning cell within the box, we found that the downward export of C_{ant}-loaded central waters in the Gulf of Cadiz, and subsequent formation of MW (between 800 to 1200 dbar) lets 74 ± 14 kmol s^{-1} of C_{ant} be drawndown from upper to intermediate ocean. In particular, the entrainment of central waters (37 ± 7 kmol s^{-1} of C_{ant}) to feed Mediterranean Outflow Water (42 ± 5 kmol s^{-1} of C_{ant}), provides the resulting MW with 79 ± 9 kmol s^{-1} of C_{ant}. Of that amount, 39 ± 9 kmol s^{-1} (net C_{ant} transport by MW across the limits of WOA09-Box) will be ultimately advected into the North Atlantic, while the remaining 40 ± 15 kmol s^{-1} will be available to contribute to the total C_{ant} storage rate within the Azores-Gibraltar Strait region.

Within the context of the entire North Atlantic, the Gulf of Cadiz represents much less than 1% of the total area, yet annually (climatological mean) the newly formed MW accounts for a C_{ant} storage rate in the North-East Atlantic of 0.020 ± 0.003 Pg-C yr^{-1}, which represents 6% of the C_{ant} storage rate in the entire subtropical North Atlantic (0.280 ± 0.011 Pg-C yr^{-1}, referenced to 2004; Pérez et al., 2013). Our results have let us firmly point to this singular region as a long-term C_{ant} sink and deep storage basin in a year-round basis. Regional estimates of the C_{ant} inventory in key regions such as the North-East Atlantic are, therefore, a significant contribution towards the refinement of the global deep CO_2 storage estimates.

While C_{ant} transports could be biased towards lower-bound estimates, due to the smoothed nature of the density field from which geostrophic velocities are derived, C_{ant} inventory/storage rate estimates have been proved to be in good agreement with previous cruise-data-based values.

Overall, we aim to highlight the suitability of the joint use of the GLODAPv2 and WOA09 databases to depict the annual mean state of the C_{ant} budget in the ocean.

Acknowledgments and Data

This work was funded by the Spanish National Research Council (CSIC), through the EU H2020 project AtlantOS (‘‘Optimizing and Enhancing the Integrated Atlantic Ocean Observing Systems Research’’, RIA), financed by the European Commission’s H2020 Framework Programme under grant agreement no. 633211. The first author is being funded by the University of Vigo, through the Galician I2C Plan for postdoctoral research. F.F. Pérez and G. Rosón were supported by the Spanish Ministry of Economy through the CATARINA (CTM2010-17141) and BOCATS (CTM2013-41048-P) projects, both co-funded by the Fondo Europeo de Desarrollo Regional (FEDER). We thank S. Torres-Valdés for the constructive feedback provided and to E. D. Barton for the English proofreading. Likewise, we gratefully acknowledge the data sources for this study: potential temperature and salinity to derive geostrophic velocity estimates, from the 2009 World Ocean Atlas (WOA09) database (Boyer et al., 2009) (http://www.nodc.noaa.gov/OC5/WOA09/), carbonate system variables to estimate C_{ant}, from the GLODAPv2 database (http://cdiac.ornl.gov/oceans/GLODAPv2/), and the pCO_2 climatology of Takahashi et al. (2009) (www.ldeo.columbia.edu).

Appendix A. Supplementary Text

A.1. The φC_T^0 method for C_{ant} estimate

The anthropogenic CO_2 in the ocean (C_{ant}) is not a tracer that can be directly measured, as both natural and anthropogenic CO_2 molecules are identical although they present different isotopic ($\delta^{13}C/\ \delta^{12}C$) ratios (Quay et al., 2007). Moreover, the anthropogenic signal is less than 1% of the oceanic CO_2 load (up to 3.5% in surface layers), thus adding difficulty to its study and accurate quantification. In the late 1970s, authors such as Brewer (1978) or Chen and Millero (1979) introduced for the first time the so-called back-calculation techniques, an indirect C_{ant} estimate based on direct measurements of total inorganic carbon (C_T), total alkalinity (A_T) and dissolved oxygen. C_{ant} is referred to as the difference between the preformed total inorganic carbon (C_T^0, note hereafter superscript 0 will mean preformed) and its concentration after the preindustrial era ($C_T^{0\pi}$). C_T^0 is determined as $C_T^0 = C_T - \Delta C_{bio,}$ where ΔC_{bio} stands for the organic matter oxidation/remineralization processes and the dissolution of $CaCO_3$; while $C_T^{0\pi}$ is determined as $C_T^{0\pi} = C_T^{eq,\pi} + \Delta C_{dis}^{\pi}$, where $C_T^{eq,\pi}$ is the total inorganic carbon in atmosphere-ocean equilibrium in the preindustrial era, and ΔC_{dis}^{π} is the disequilibrium in the atmosphere-ocean interphase.

From the early approaches, back-calculation techniques were subject to various improvements, one of the most recent being the so-called φC_T^0 method (Vázquez-Rodríguez et al., 2009b, see their Eq.10). The φC_T^0 method was developed under the assumption that biogeochemical processes that modulate oceanic C_T have operated invariably with time. The method, which shares principles with the more classical ΔC^* method of Gruber et al. (1996), proposes different parameterizations to calculate ΔC_{dis} and the preformed alkalinity (A_T^0) to assess the contribution of $CaCO_3$ dissolution to C_T. A_T^0 is based on the concept of potential alkalinity PA_T and is defined as $A_T^0 = PA_T - (NO_3^0 + PO_4^0)$ (Vázquez-Rodríguez et al., 2012), where NO_3^0 and PO_4^0 are determined as $NO_3^0 = NO_3 – AOU/R_{ON}$ and $PO_4^0 = PO_4 – AOU/R_{OP}$. AOU stands for Apparent Oxygen Utilisation, that is, the difference between the saturated concentrations of oxygen (Benson and Krause, 1984) and the measured concentrations of oxygen; and R_{ON} and R_{OP} are the Redfield ratios proposed by Anderson and Sarmiento (1994), satisfactorily applied in the North Atlantic for the estimate of C_{ant} by, e.g., Pérez et al. (2008; 2010; 2013) or Ríos et al. (2012, 2015). A relevant aspect of the φC_T^0 method parameterizations is that they are not CFC-reliant (i.e., there is no need of arbitrary references for C_{ant}=0 based on CFCs measurements). Instead, the φC_T^0 method uses conservative properties of the subsurface layer (100–200 m) from the whole Atlantic to build these parametrizations. In their study, Vázquez-Rodríguez et al. (2009a) used 10 WOCE cruises along the Atlantic spanning between 1993 and 2003, for which CFC-11 and CFC-12 measurements were available, to apply a shortcut method (Thomas and Ittekkot, 2001) for the estimate of C_{ant} in waters θ>5ºC. Since the average age of the water masses in the Atlantic 100–200m depth domain is under 25 years, the use of a shortcut method is considered to be appropriate (Matear et al., 2003). With the shortcut-based C_{ant} estimates, and the additional measurements of temperature, salinity, C_T, A_T, and AOU, ΔCdis is parametrized by means of multilinear regressions. Once parametrized, ΔCdis can therefore be estimated without further need of CFC data. For waters θ<5ºC, the MLR parametrization is substituted by an Optimum Multiparameter Analysis (Vázquez et al., 2009a). This procedure lets the improvement of C_{ant} estimations in cold deep waters where complex-mixing processes between northern and southern hemispheric source water masses takes place. The overall uncertainty of the φC_T^0 method is ±5.2 μmol kg^{-1}, as computed by Vázquez-Rodríguez et al. (2009b) by random propagation of the errors associated with the input variables necessary to apply the method. This value was used in this study to perform a perturbation analysis of uncertainties (see Appendix A3).

Several intercomparison studies in the Atlantic Ocean support the robustness and validity of the φC_T^0 method (Ríos et al., 2001, 2010; Álvarez et al., 2005; Pérez et al., 2010; Fajar et al., 2012; Flecha et al., 2012). Further details of the method can be found in Vázquez-Rodríguez et al. (2009b), and the Matlab® code is freely available on the IIM-CSIC CO_2 Group webpage (http://oceano.iim.csic.es/co2group/index.html).

In the current study, we applied the φC_T^0 back-calculation technique to GLODAPv2 bottle data (http://cdiac.ornl.gov/ftp/oceans/GLODAPv2/Data_Products/data_product/). C_{ant} estimates were scaled from their original cruise year ($C_{ant}(t1)$) to year 2000 ($C_{ant}(t2)$) using the transient steady state approach (Tanhua et al., 2006). We selected year 2000 as reference to be concordant with the pCO_2 climatology of Takahashi et al. (2009) (dataset used in this study to estimate the air-sea CO_2 flux, section 2.4). C_{ant} concentrations were time-normalized following:

$$C_{ant}(t2)=C_{ant}(t_1)\ (1+k_t)^{(t2-t1)} \qquad \text{(A1)}$$

where *t1* corresponds to each GLODAPv2 cruise occupation year; *t2* is the reference year 2000; and k_t is the annual C_{ant} rate of increase (k_t = 0.0169 ± 0.001 y^{-1}, Steinfeldt et al. (2009)). Normalizing C_{ant} estimates to a year of reference ensures a time homogeneous recordset, whereas it just entails a minor correction, that is, it only accounts for 1.7% of the value of C_{ant} for each year of difference with an error of 0.1% (Guallart et al. 2015). Note this error is two orders of magnitude smaller than the 10% of error associated to the C_{ant} transport estimate (Appendix A.2.1).

A.2. Uncertainty estimate

A.2.1. C_{ant} transport

Tracer transports come from the product of volume fluxes and the tracer concentration. The error associated to any transport can be computed by applying the error propagation formula (Eq. A2). Being $F=f(x_1, x_2, ..., x_N)$, and assuming a zero-correlation between the independent variables, the error propagation formula is:

$$\varepsilon=\left[\left(\frac{\partial F}{\partial x_1}\right)^2 \varepsilon_1^2+\left(\frac{\partial F}{\partial x_2}\right)^2 \varepsilon_2^2+\ldots+\left(\frac{\partial F}{\partial x_N}\right)^2 \varepsilon_N^2\right]^{1/2} \quad \text{(A2)}$$

In view of that, the error of the C_{ant} transport can be computed as the sum of errors due to both the mass transport (transport-derived uncertainty, $\sigma T_{Cant}{}^{T}$) and the C_{ant}concentrations (C_{ant}-derived uncertainty, $\sigma T_{Cant}{}^{Cant}$), such as:

$$\varepsilon=\sqrt{\left(\sigma T_{Cant}^{T}\right)^2+\left(\sigma T_{Cant}^{Cant}\right)^2} \quad \text{(A3)}$$

$\sigma T_{Cant}{}^{T}$ was calculated from the covariance matrix of errors for mass transport (diagonal matrix of covariance at the reference level for all station pairs), as obtained from the two-dimensional geostrophic inverse ocean model (Carracedo et al., 2014). On the other hand, $\sigma T_{Cant}{}^{Cant}$ was estimated as the product of the net transport across the subregion considered and the standard deviation of the C_{ant} concentration at the same subregion.

To illustrate this, we show as an example the uncertainty estimate for the net C_{ant} transport across the WOA09-Box. Following the error propagation formula (Eq. A3), this results in:

$$\varepsilon T_{Box}\mathbf{C}_{ant}=\sqrt{\left[\sigma T_{Cant}^{T}\right]^2+\left[std(C_{ant})\times T_{Box}\right]^2}=$$

$$=\sqrt{[14.0]^2+[0.17]^2}=14\ \text{kmols}^{-1}$$

Where std(C_{ant}) refers to the standard deviation of C_{ant} in the section (std(C_{ant})=14.8 µmol kg^{-1}, that is 1.52x10^{-5} kmol m^{-3}, by multiplying by a reference density for seawater of 1026 kg m^{-3}), and T_{Box} (0.011x10^{6} m^{3} s^{-1}) refers to the net volume transport across the box.

A.2.2. C_{ant} storage rate

Vázquez Rodríguez et al. (2009a) and Pérez et al. (2013) calculated the uncertainty related to the C_{ant} inventory estimate by randomly propagating over depth a 5 µmol kg^{-1} standard error for C_{ant}. They obtained values of ±1 mol-C m^{-2} and ±2 mol-C m^{-2} when integrated down to 3000 m and 6000 m, respectively. By applying that ±2 mol m^{-2} uncertainty to the WOA09-Box area, we obtained a total value of ± 9 kmol s^{-1}.

A.2.3. Air-sea CO_2 and C_{ant} flux

The uncertainty estimate for the air-sea CO_2 flux was given as the mean standard error of the monthly $F_{Air\text{-}sea}CO_{2i}$ (with i=1...12) estimate within the WOA09-Box:

$$\varepsilon F_{Air\text{-}sea}CO_2 = \frac{std(F_{Air\text{-}sea}CO_{2_i})}{\sqrt{12}} = \frac{26.1}{\sqrt{12}} = 8 \text{ kmol s}^{-1} \quad \text{(A4)}$$

The air-sea C_{ant} flux, $F_{Air\text{-}sea}C_{ant}$, is the result from equation (5), so its uncertainty was estimated by means of error propagation (Eq. A2), such as:

$$\varepsilon F_{Air\text{-}sea}C_{ant} = \sqrt{(\varepsilon C_{ant} \text{storage rate})^2 + (\varepsilon T_{Strait}C_{ant})^2 + (\varepsilon_G T_{Box}C_{ant})^2}$$

$$= \sqrt{(9)^2+(1)^2+(5)^2} = 6 \text{ kmols}^{-1} \quad \text{(A5)}$$

εC_{ant} storage rate is the value obtained in section A.2.2; $\varepsilon T_{Strait}C_{ant}$ is the value estimated by (Huertas et al., 2009); and, finally, $\varepsilon_G T_{Box}C_{ant}$ corresponds to the uncertainty estimate of the net C_{ant} transport for the WOA09-Box. With the particular purpose of providing a tighter final uncertainty to the $F_{Air\text{-}sea}C_{ant}$ estimate, we recalculated a new uncertainty for the $T_{Box}C_{ant}$ term, $\varepsilon_G T_{Box}C_{ant}$, according to Ganachaud et al. (2000), such as:

$$\varepsilon_G T_{Box}C_{ant} = \sum_{i=1}^{n \text{ layers}} \sqrt{4 \times \sigma T_{Box\ i}{}^2 \times std(C_{ant\ i})^2} = 5 \text{ kmols}^{-1}$$

Where $\varepsilon_G T_{Box}C_{an}$ was given as the sum of the tracer transport uncertainties by horizontal layers. In the equation, the factor 4 aims to account for possible correlations between the zonal average and horizontal eddy component (Ganachaud et al., 2000).

A.3. Robustness of C_{ant} transports: perturbation analysis

In section A2, the uncertainty estimates were based on the assumption that errors are independent of one another. As this assumption may be questionable, we performed a perturbation analysis of uncertainties (Lawson and Hanson, 1974) to validate whether uncertainties were being underestimated and, at the same time, to check the robustness of our results. Final uncertainties were computed here as the standard deviation of an ensemble generated by random perturbation of the C_{ant} transports.

A.3.1. Perturbed C_{ant} transports

As shown in equation (1), the transport of C_{ant} comes from the combination (product) of the absolute velocities and C_{ant} concentrations. Both data fields are obtained following two different methodologies: *i)* water property inversion estimating the volumetric transports (in this study, a result by Carracedo et al. 2014); and *ii)* back-calculation of C_{ant} based on water properties (as explained in A.1). If, in addition, we want to provide the C_{ant} transport by water mass, as shown in equation (3), a third factor takes part: the water mass mixing fractions*,* obtained by means of an OMP analysis (in this study, a result by Carracedo et al. 2014).

The procedure followed for the perturbation analysis consisted of re-computing the transport of C_{ant} from 100 randomly perturbed fields of velocity, C_{ant} and water fractions (test 1). To test which of the perturbed fields (velocity, C_{ant} of water masses fractions) influences the results the most, we also re-estimated the C_{ant} transports by perturbing just one of the factors each time, that is, we estimated the C_{ant} transports:

a) test 2: from 100 randomly perturbed velocity fields (no perturbed C_{ant} or water mass fractions)
b) test 3: from 100 randomly perturbed C_{ant} fields (no perturbed velocities or water mass fractions (test 3)
c) test 4: from 100 randomly perturbed water mass fractions (no perturbed velocities or C_{ant})

To perturb any of the variables, we assumed they followed a normal distribution, so that the perturbation process lay in varying the property values according to a normal distribution within a given range.

As for the velocity field, we based on the inverse model surface-to-bottom mass conservation constraint (Tr_{net}=0.01 ± 1 Sv, Carracedo et al. 2014), to ensure the perturbed velocity field was consistent with mass conservation. We randomly perturbed the net volume transport across the section with zero mean and standard deviation of 1 Sv, obtaining a cross-section perturbed velocity v_p of: $v_p = (Tr_{net})_{perturbed}/$ total section area. This velocity was (zonally and vertically) uniformly added to the velocity field, so that the perturbed velocity field was still consistent with mass conservation.

C_{ant} concentrations were randomly perturbed with zero mean and standard deviation of 5.2 μmol kg^{-1}, being 5.2 μmol kg^{-1} the overall uncertainty for the C_{ant} estimates (Vázquez-Rodríguez et al., 2009b).

As for the water mixing fractions, both the properties of each water sample and of each source water type (also referred to as source water mass, SWM) were perturbed. In terms of the OMP analysis, the SWMs are points in the *n*-dimensional parameter space (*n* is the number of properties that characterize SWMs) (Tomczak, 1981). In the study of Carracedo et al. (2014), the SWMs were characterized by θ, S, O_2^0, NO_3^0, PO_4^0 and $Si(OH)_4^0$ (where the superscript 0 means preformed variables) (see Table A2). The properties of each SWM were randomly modified with the mean being the value of the property, and the standard deviation (STD), the values given by Álvarez et al (2005) for θ and S, and a percentage of their value for O_2 (1% of the property value) and nutrients (2% of the property value) (Table A2). The perturbation of the water sample properties were performed with the mean equal to the property value at each point and the standard deviation equal to the accuracy of each water sample property (ε, Table A2). 100 perturbations were done and the OMP analysis was solved for each perturbed system. Uncertainties for the SWMs contributions were computed as the standard deviation of the 100 water mass distribution matrices. The mean standard distribution (referred to as uncertainty) is shown in Table A2.

Table A2. Main properties of each of the Source Water Masses (SWMs) considered in the eOMP analysis by Carracedo et al. (2014), with their correspondent standard deviation (STD). Note that what we refer to as Central Waters (CW) in the present study is the sum of MMW, $ENACW_T$ and $ENACW_P$. Accuracies of the measured properties, ε, used to compute the perturbation of the tracer fields are also shown. The last column accounts for the uncertainties in the SWMs contributions, that is, the mean of the standard deviation of the 100 perturbations (values expressed on a per one basis).

	Potential Temperature (θ^{SWT})	Salinity (S^{SWT})	Silicate ($Si(OH)_4^{0\ SWT}$)	Nitrate ($NO_3^{0\ SWT}$))	Phosphate ($PO_4^{0\ SWT}$)	Oxygen ($O_2^{\ SWT}$)	Uncertainty
	°C	*psu*	*µmol kg-1*				*Parts per unit*
MMW	20.0±0.5	37.00±0.04	0±0	0±0	0±0	223±2	0.03
$ENACW_T$	15.3±0.4	36.10±0.02	2.05±0.04	1.23±0.02	0.136±0.003	244±2	0.04
$ENACW_P$	8.3±0.3	35.23±0.01	9.8±0.2	11.1±0.2	1.10±0.02	304±3	0.05
MW	11.7±0.1	36.50±0.01	9.1±0.2	4.0±0.1	0.31±0.01	261±3	0.02
AAIW	7.5±0.1	35.00±0.02	24.8±0.5	16.2±0.3	0.95±0.02	290±3	0.04
LSW	3.4±0.2	34.89±0.12	9.1±0.2	12.5±0.2	0.94±0.02	325±3	0.03
ISOW	2.5±0.1	34.98±0.02	13.8±0.3	7.1±0.1	0.60±0.01	319±3	0.01
$NEADW_L$	1.920±0.003	34.885±0.002	50.0±1.0	13.6±0.3	0.95±0.02	337±3	0.02
ε	0.005	0.005	0.5	0.2	0.002	3.3	-

To illustrate the results of the perturbation analysis, we recomputed as an example the net C_{ant} transport across the section, $T_{Box}C_{ant}$, for the 4 different tests (100 perturbations each test) and calculated the standard deviation of the 100 values per test (see Table A3). More than 80% of the C_{ant} transport error estimate is due to the velocity field, whereas C_{ant} concentration uncertainty just accounts for less than 20% of the total error. If we consider the C_{ant} transport by water masses, then the water masses contribution accounts for around 65% of the total error, velocity field for 25% and C_{ant} concentrations for 10-15%.

By comparing the uncertainty estimates from the perturbation analysis with the uncertainty estimates from the error propagation formula (as explained in Section A2), we see the former are smaller than the latter. In view of that, we took the uncertainties obtained by error propagation, that is, the largest ones, as those accompanying our results in the manuscript.

Table A3. Standard deviation of the 100-times perturbed net C_{ant} transports for each of the 4 tests performed. In parenthesis, percentage of the total uncertainty represented by each of the variables (v, C_{ant} or WMs). *v* refers to the velocity field, C_{ant} to the C_{ant} concentrations; WMs to the water masses contribution; CW to Central waters; MW to Mediterranean Water.

Perturbation Analysis			
Perturbed field	Net C_{ant} transport (kmol/s)		
	Total	Net by CW	Net by MW
test 1: *v*, C_{ant}, WMs	± 4	± 3	± 1

test 2:	*v*	± 4 (82%)	± 1 (22%)	± 0.5 (27%)
test 3:	C_{ant}	± 0.8 (18%)	± 0.6 (14%)	± 0.1 (7%)
test 4:	WMs	-	± 3 (64%)	± 1 (65%)
		Error Propagation		
(see A.2)		± 14	± 18	± 8

A.3.2. Perturbed Air-sea C_{ant} flux

$F_{Air\text{-}sea}C_{ant}$ is estimated (Eq. 6) as the difference between the C_{ant} *storage rate* and the C_{ant} being advected across the walls of the enclosed box ($T_{Box}C_{ant}$ + $T_{Strait}C_{ant}$). Therefore, the perturbation procedure consisted in re-estimating $F_{Air\text{-}sea}C_{ant}$ by perturbing independently each of the terms to be summed up as follows: i) C_{ant} *storage rate:* We recomputed the C_{ant} *inventory* by randomly perturbing C_{ant} concentrations according to a normal distribution with zero mean and standard deviation of 5.2 µmol kg^{-1} (Vázquez-Rodríguez et al., 2009b); ii) $T_{Box}C_{ant}$*:* We used the estimates from the "test 1" perturbation analysis (see previous section); iii) $T_{Strait}C_{ant}$: we randomly perturbed this value by following a normal distribution with mean 11 kmol s^{-1} and standard deviation 1 kmol s^{-1}.

The standard deviation of the ensemble of 100 $F_{Air\text{-}sea}C_{ant}$ estimates was 4 kmol s^{-1}, an uncertainty smaller than that obtained by error propagation (10 kmol s^{-1}, section A2.3). So once again, we kept the largest uncertainty as the most suitable one.

Appendix B. Supplementary Figures

Supplementary figures associated with this article can be found in the online version.

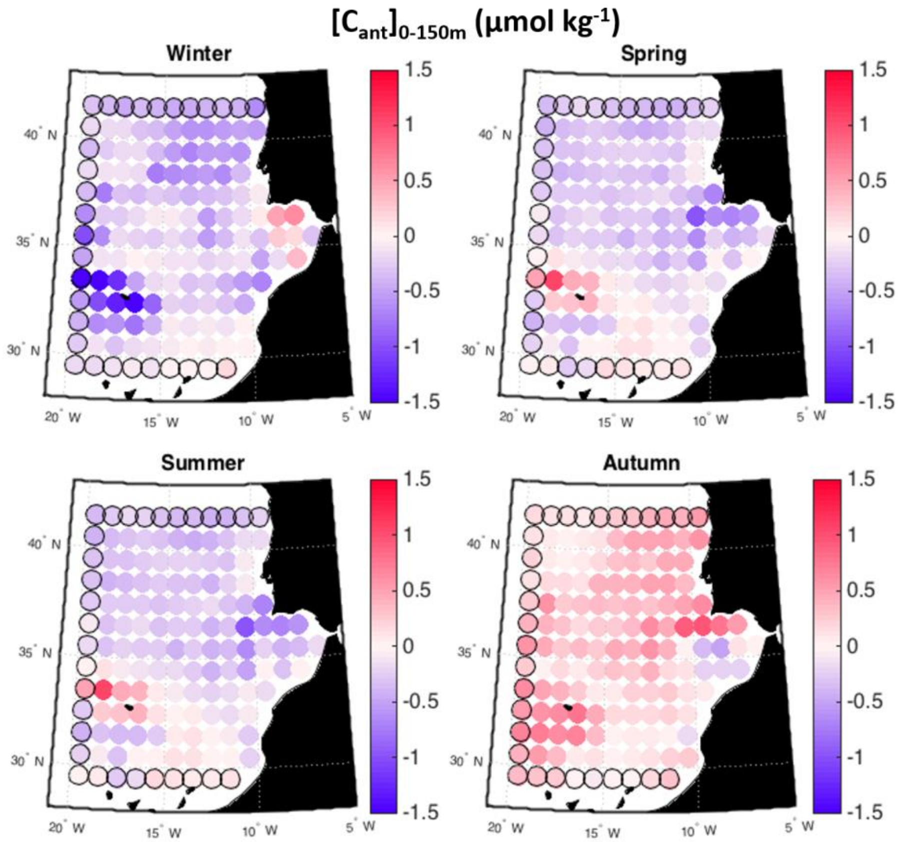

Figure B1. a) Seasonal distribution maps of C_{ant} anomalies in the upper 150 m of the water column. Anomalies are estimated as the seasonal C_{ant} concentration averaged in the upper 150 m minus the annual C_{ant} concentration averaged in the upper 150 m.

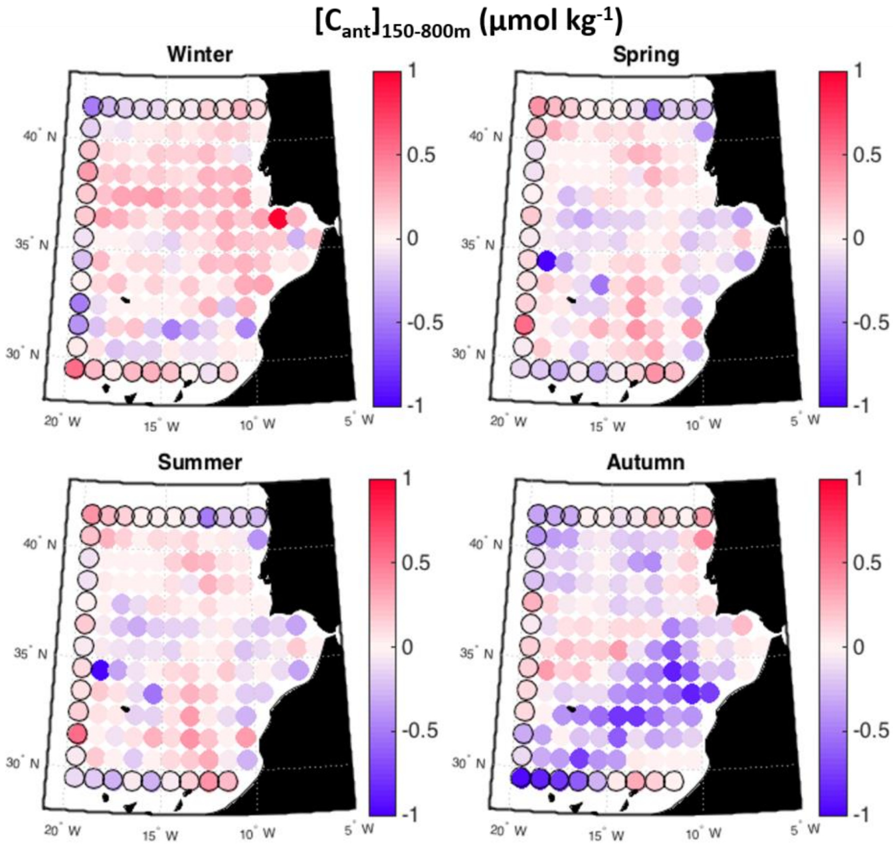

Figure B1. b) Seasonal distribution maps of C_{ant} anomalies between 150-800 m. Anomalies are estimated as the seasonal C_{ant} concentration averaged between 150-800 m minus the annual C_{ant} concentration averaged between 150-800 m.

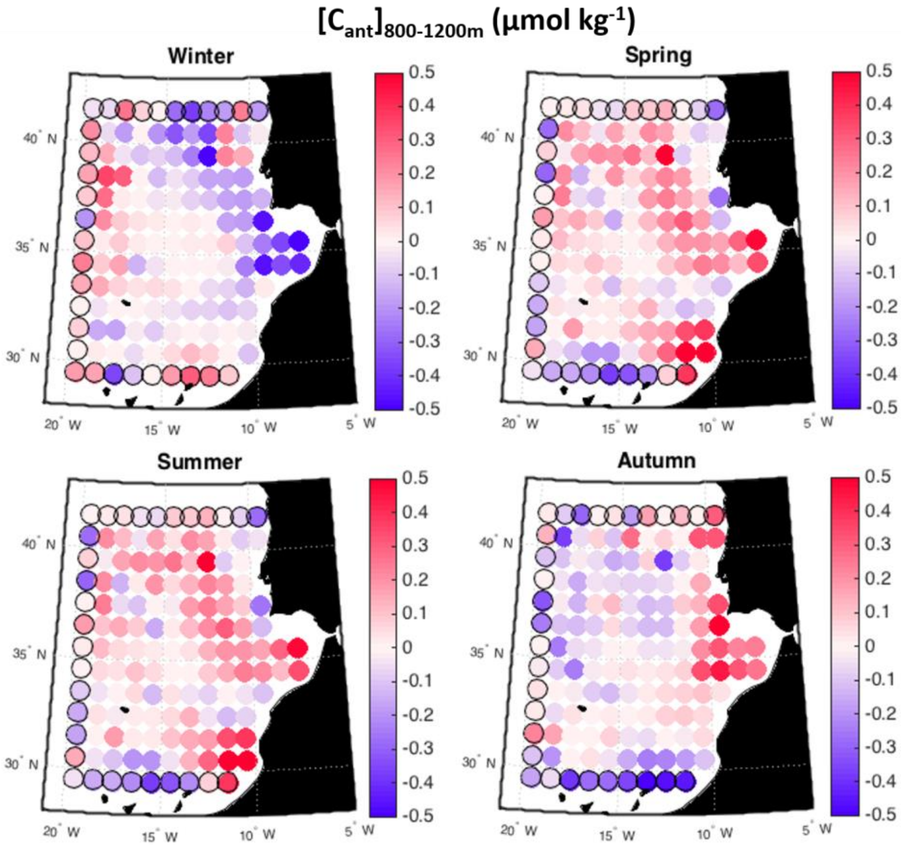

Figure B1. c) Seasonal distribution maps of C_{ant} anomalies between 800-1200 m. Anomalies are estimated as the seasonal C_{ant} concentration averaged between 800-1200 m minus the annual C_{ant} concentration averaged between 800-1200 m.

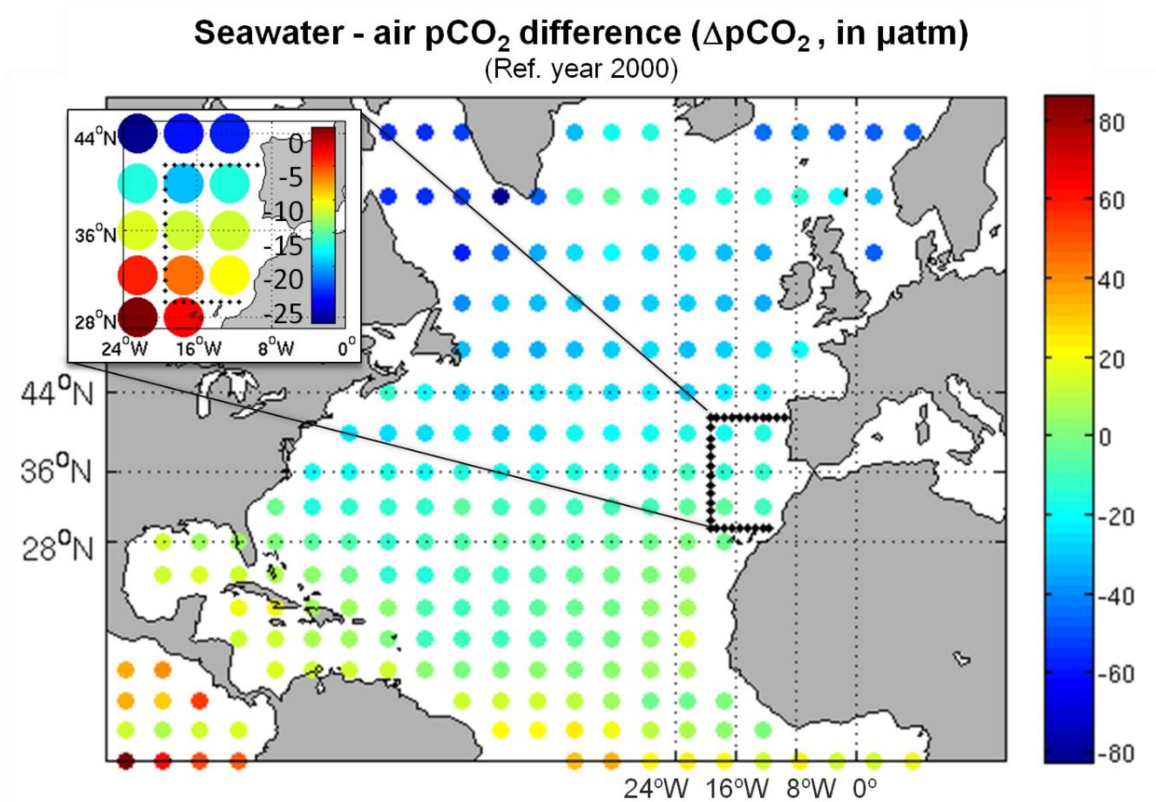

Figure B2. Distribution maps of the climatological annual mean of the air-sea difference in CO_2 partial pressure (4° Latitude x 5° Longitude).

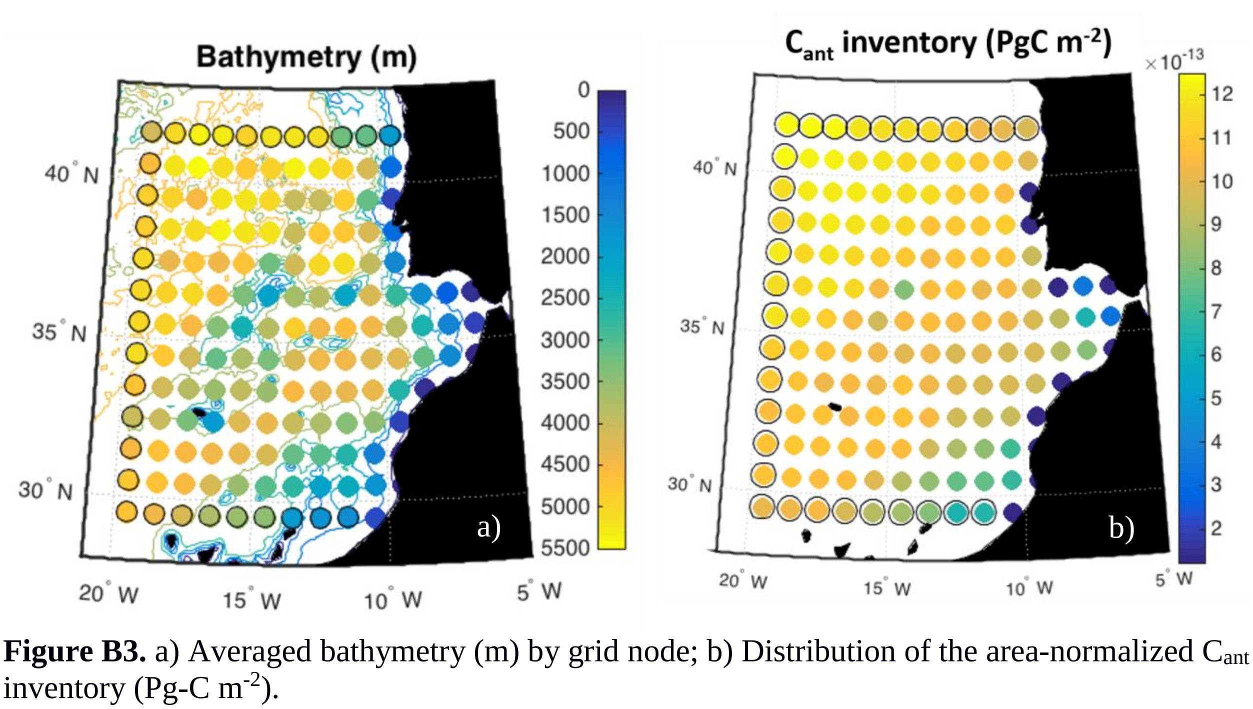

Figure B3. a) Averaged bathymetry (m) by grid node; b) Distribution of the area-normalized C_{ant} inventory (Pg-C m^{-2}).

References

Aït-Ameur, N., Goyet, C., 2006. Distribution and transport of natural and anthropogenic CO2 in the Gulf of Cadiz. Deep Sea Res. Part II Top. Stud. Oceanogr., The Gulf of Cadiz Oceanography: A Multidisciplinary View The Gulf of Cadiz Oceanography: A Multidisciplinary View 53, 1329–1343. doi:10.1016/j.dsr2.2006.04.003.

Álvarez, M., Pérez, F.F., Shoosmith, D.R., Bryden, H.L., 2005. Unaccounted role of Mediterranean Water in the drawdown of anthropogenic carbon. J. Geophys. Res. 110. doi:10.1029/2004JC002633

Anderson, L.A., Sarmiento, J.L., 1994. Redfield ratios of remineralization determined by nutrient data analysis. Glob. Biogeochem Cycles 8, 65–80. doi:10.1029/93GB03318.

Barbosa Aguiar, A.C., Péliz, A., Neves, F., Bashmachnikov, I., Carton, X., 2015. Mediterranean outflow transports and entrainment estimates from observations and high-resolution modelling. Prog. Oceanogr. 131, 33–45. doi:10.1016/j.pocean.2014.11.008.

Benson, B.B., Krause, D., 1984. The concentration and isotopic fractionation of oxygen dissolved in freshwater and seawater in equilibrium with the atmosphere. Limnol. Oceanogr. 29, 620–632.

Boyer, T.P., Antonov, J.I., Baranova, O.K., Garcia, H.E., Johnson, D.R., Locarnini, R.A., Mishonov, A.V., Seidov, D., Smolyar, I.V., Zweng, M.M., 2009. World Ocean Database 2009, Chapter 1: Introduction, Levitus, S. ed. Washington, D. C.

Brewer, P.G., 1978. Direct observation of the oceanic CO2 increase. Geophys. Res. Lett. 5, 997–1000. doi:10.1029/GL005i012p00997

Broecker, W.S., 1974. “NO”, a conservative water-mass tracer. Earth Planet. Sci. Lett. 23, 100–107. doi:10.1016/0012-821X(74)90036-3.

Carracedo, L.I., Gilcoto, M., Mercier, H., Pérez, F.F., 2014. Seasonal dynamics in the Azores–Gibraltar Strait region: A climatologically-based study. Prog. Oceanogr. 122, 116–130. doi:10.1016/j.pocean.2013.12.005.

Carracedo, L.I., Gilcoto, M., Mercier, H., Pérez, F.F., 2015. Quasi-synoptic transport, budgets and water mass transformation in the Azores–Gibraltar Strait region during summer 2009. Prog. Oceanogr. 130, 47–64. doi:10.1016/j.pocean.2014.09.006.

Carracedo, L.I., Pardo, P.C., Flecha, S., Pérez, F.F., 2016. On the Mediterranean Water Composition. J. Phys. Oceanogr. 46, 1339–1358. doi:10.1175/JPO-D-15-0095.1.

Chen, G.T., Millero, F.J., 1979. Gradual increase of oceanic CO_2. Nature 277, 205–206. doi:10.1038/277205a0

Fajar, N.M., Pardo, P.C., Carracedo, L., Vázquez-Rodríguez, M., Ríos, A.F., Pérez, F.F., 2012. Trends of anthropogenic CO_2 along 20^{o} W in the Iberian Basin. Cienc. Mar. 38, 287–306.

Fajar, N.M., Guallart, E.F., Steinfeldt, R., Ríos, A.F., Pelegrí, J.L., Pelejero, C., Calvo, E., Pérez, F.F., 2015. Anthropogenic CO_2 changes in the Equatorial Atlantic Ocean. Prog. Oceanogr. 134, 256–270. doi:10.1016/j.pocean.2015.02.004.

Flecha, S., Pérez, F.F., Navarro, G., Ruiz, J., Olivé, I., Rodríguez-Gálvez, S., Costas, E., Huertas, I.E., 2012. Anthropogenic carbon inventory in the Gulf of Cadiz. J. Mar. Syst. 92, 67–75. doi:10.1016/j.jmarsys.2011.10.010.

Fusco, G., Artale, V., Cotroneo, Y., Sannino, G., 2008. Thermohaline variability of Mediterranean Water in the Gulf of Cadiz, 1948–1999. Deep Sea Res. Part Oceanogr. Res. Pap. 55, 1624–1638. doi:10.1016/j.dsr.2008.07.009.

Ganachaud, A., Wunsch, C., Marotzke, J., Toole, J., 2000. Meridional overturning and large-scale circulation of the Indian Ocean. J. Geophys. Res. 105, 26117–26,134. doi:10.1029/2000JC900122.
Gourcuff, C., Lherminier, P., Mercier, H., Le Traon, P.Y., 2011. Altimetry Combined with Hydrography for Ocean Transport Estimation. J. Atmospheric Ocean. Technol. 28, 1324–1337. doi:10.1175/2011JTECHO818.1.
Gruber, N., Sarmiento, J.L., Stocker, T.F., 1996. An improved method for detecting anthropogenic CO_2 in the oceans. Glob. Biogeochem. Cycles 10, 809–837. doi:10.1029/96GB01608
Huertas, I.E., Ríos, A.F., García-Lafuente, J., Makaoui, A., Rodríguez-Gálvez, S., Sánchez-Román, A., Orbi, A., Ruiz, J., Pérez, F.F., 2009. Anthropogenic and natural CO_2 exchange through the Strait of Gibraltar.
Keeling, C.D., Bolin, B., 2010. The simultaneous use of chemical tracers in oceanic studies I. General theory of reservoir models1,2. Tellus 19, 566–581. doi:10.1111/j.2153-3490.1967.tb01509.x.
Key, R.M., Olsen, A., van Heuven, S., Lauvset, S.K., Velo, A., Lin, X., Schirnick, C., Kozyr, A., Tanhua, T., Hoppema, M., Jutterstrom, S., Steinfeldt, R., Jeansson, E., Ishi, M., Perez, F.F., Suzuki, T., 2015. Global Ocean Data Analysis Project, Version 2 (GLODAPv2), ORNL/CDIAC-162, ND-P093. Carbon Dioxide Information Analysis Center (CDIAC).
Le Quéré, C., Moriarty, R., Andrew, R.M., Canadell, J.G., Sitch, S., Korsbakken, J.I., Friedlingstein, P., Peters, G.P., Andres, R.J., Boden, T.A., Houghton, R.A., House, J.I., Keeling, R.F., Tans, P., Arneth, A., Bakker, D.C.E., Barbero, L., Bopp, L., Chang, J., Chevallier, F., Chini, L.P., Ciais, P., Fader, M., Feely, R.A., Gkritzalis, T., Harris, I., Hauck, J., Ilyina, T., Jain, A.K., Kato, E., Kitidis, V., Klein Goldewijk, K., Koven, C., Landschützer, P., Lauvset, S.K., Lefèvre, N., Lenton, A., Lima, I.D., Metzl, N., Millero, F., Munro, D.R., Murata, A., Nabel, J.E.M.S., Nakaoka, S., Nojiri, Y., O'Brien, K., Olsen, A., Ono, T., Pérez, F.F., Pfeil, B., Pierrot, D., Poulter, B., Rehder, G., Rödenbeck, C., Saito, S., Schuster, U., Schwinger, J., Séférian, R., Steinhoff, T., Stocker, B.D., Sutton, A.J., Takahashi, T., Tilbrook, B., van der Laan-Luijkx, I.T., van der Werf, G.R., van Heuven, S., Vandemark, D., Viovy, N., Wiltshire, A., Zaehle, S., Zeng, N., 2015. Global Carbon Budget 2015. Earth Syst. Sci. Data 7, 349–396. doi:10.5194/essd-7-349-2015.
Lee, K., Choi, S.D., Park, G.H., Wanninkhof, R., Peng, T.H., Key, R.M., Sabine, C.L., Feely, R.A., Bullister, J.L., Millero, F.J., 2003. An updated anthropogenic CO2 inventory in the Atlantic Ocean. Glob. Biogeochem. Cycles 17, 1116. doi:10.1029/2003GB002067.
Lherminier, P., Mercier, H., Gourcuff, C., Alvarez, M., Bacon, S., Kermabon, C., 2007. Transports across the 2002 Greenland-Portugal Ovide section and comparison with 1997. J. Geophys. Res. 112, C07003.ç
Lherminier, P., Mercier, H., Huck, T., Gourcuff, C., Perez, F.F., Morin, P., Sarafanov, A., Falina, A., 2010. The Atlantic Meridional Overturning Circulation and the subpolar gyre observed at the A25-OVIDE section in June 2002 and 2004. Deep Sea Res. Part Oceanogr. Res. Pap. 57, 1374–1391. doi:10.1016/j.dsr.2010.07.009.
Lønborg, C., Álvarez-Salgado, X.A., 2014. Tracing dissolved organic matter cycling in the eastern boundary of the temperate North Atlantic using absorption and fluorescence spectroscopy. Deep Sea Res. Part Oceanogr. Res. Pap. 85, 35–46. doi:10.1016/j.dsr.2013.11.002.

Mercier, H., 1986. Determining the general circulation of the ocean: A nonlinear inverse problem. J. Geophys. Res. Oceans 91, 5103–5109.

Olsen, A., Key, R.M., van Heuven, S., Lauvset, S.K., Velo, A., Lin, X., Schirnick, C., Kozyr, A., Tanhua, T., Hoppema, M., Jutterström, S., Steinfeldt, R., Jeansson, E., Ishii, M., Pérez, F.F., Suzuki, T., 2016. The Global Ocean Data Analysis Project version 2 (GLODAPv2) – an internally consistent data product for the world ocean. Earth Syst. Sci. Data 8, 297–323. doi:10.5194/essd-8-297-2016.

Pardo, P.C., Pérez, F.F., Velo, A., Gilcoto, M., 2012. Water masses distribution in the Southern Ocean: Improvement of an extended OMP (eOMP) analysis. Prog. Oceanogr. 103, 92–105. doi:10.1016/j.pocean.2012.06.002.

Pérez, F.F., Vázquez-Rodríguez, M., Louarn, E., Padín, X.A., Mercier, H., Ríos, A.F., 2008. Temporal variability of the anthropogenic CO2 storage in the Irminger Sea. Biogeosciences 5, 1669–1679.

Pérez, F.F., Arístegui, J., Vázquez-Rodríguez, M., Ríos, A.F., 2010. Anthropogenic CO2 in the Azores region. Sci. Mar. 74, 11–19. doi:10.3989/scimar.2010.74s1011.

Pérez, F.F., Mercier, H., Vázquez-Rodríguez, M., Lherminier, P., Velo, A., Pardo, P.C., Rosón, G., Ríos, A.F., 2013. Atlantic Ocean CO2 uptake reduced by weakening of the meridional overturning circulation. Nat. Geosci. 6, 146–152. doi:10.1038/ngeo1680.

Quay, P., Sonnerup, R., Stutsman, J., Maurer, J., Körtzinger, A. Padin, X. A., Robinson, C., 2007. Anthropogenic CO_2 accumulation rates in the North Atlantic Ocean from changes in the $^{13}C/^{12}C$ of dissolved inorganic carbon. Global Biogeochem. Cycles, 21, GB1009. doi:10.1029/2006GB002761.

Rhein, M., Rintoul, S.R., Aoki, S., Campos, E., Chambers, D., Feely, R.A., Gulev, S., Johnson, G.C., Josey, S.A., Kostianoy, A., Mauritzen, C., Roemmich, D., Talley, L.D., Wang, F., 2013. Observations: Ocean, in: Climate Change 2013: The Physical Science Basis. Contribution of Working Group I to the Fifth Assessment Report of the Intergovernmental Panel on Climate Change. [Stocker, T.F., D. Qin, G.-K. Plattner, M. Tignor, S.K. Allen, J. Boschung, A. Nauels, Y. Xia, V. Bex and P.M. Midgley (Eds.)]. Cambridge University Press, Cambridge, United Kingdom and New York, NY, USA. Cambridge University Press, Cambridge, Uited Kingdom and New York, NY, USA, pp. 255–316.

Ribas-Ribas, M., Gómez-Parra, A., Forja, J.M., 2011. Air–sea CO_2 fluxes in the north-eastern shelf of the Gulf of Cadiz (southwest Iberian Peninsula). Mar. Chem. 123, 56–66. doi:10.1016/j.marchem.2010.09.005.

Ríos, A.F., Pérez, F.F., Fraga, F., 2001. Long-term (1977–1997) measurements of carbon dioxide in the Eastern North Atlantic: evaluation of anthropogenic input. Deep Sea Res. Part II Top. Stud. Oceanogr., JGOFS Research in the North Atlantic Ocean: A Decade of Research, Synthesis and modelling 48, 2227–2239. doi:10.1016/S0967-0645(00)00182-X.

Ríos, A.F., Vázquez-Rodríguez, M., Padín, X.A., Pérez, F.F., 2010. Anthropogenic carbon dioxide in the South Atlantic western basin. J. Mar. Syst. 83, 38–44. doi:10.1016/j.jmarsys.2010.06.010.

Ríos, A.F., Velo, A., Pardo, P.C., Hoppema, M., Pérez, F.F., 2012. An update of anthropogenic CO_2 storage rates in the western South Atlantic basin and the role of Antarctic Bottom Water. Journal of Marine Systems 94, 197–203.

Ríos, A. F., Resplandy, L., García-Ibáñez, M. I., Fajar, N. M., Velo, A., Padin, X. A., Pérez, F. F., 2015. Decadal acidification in the water masses of the Atlantic Ocean. Proceedings of the National Academy of Sciences of the United States of America, 112(32), 9950–9955. http://doi.org/10.1073/pnas.1504613112.

Sabine, C.L., Feely, R.A., Gruber, N., Key, R.M., Lee, K., Bullister, J.L., Wanninkhof, R., Wong, C.S., Wallace, D.W.R., Tilbrook, B., Millero, F.J., Peng, T.-H., Kozyr, A., Ono, T., Rios, A.F., 2004. The Oceanic Sink for Anthropogenic CO_2. Science 305, 367–371. doi:10.1126/science.1097403.

Soto-Navarro, J., Criado-Aldeanueva, F., García-Lafuente, J., Sánchez-Román, A., 2010. Estimation of the Atlantic inflow through the Strait of Gibraltar from climatological and in situ data. J. Geophys. Res. 115. doi:10.1029/2010JC006302.

Speth, P., Detlefsen, H., Sierts, H.-W., 1978. Meteorological influence on upwelling off Northwest Africa. Dtsch. Hydrogr. Z. 31, 95–104. doi:10.1007/BF02227007.

Steinfeldt, R., Rhein, M., Bullister, J.L., Tanhua, T., 2009. Inventory changes in anthropogenic carbon from 1997–2003 in the Atlantic Ocean between 20°S and 65°N. Glob. Biogeochem. Cycles 23, GB3010. doi:10.1029/2008GB003311.

Stocker, T.F., Qin, D., Plattner, G.-K., Tignor, M., Allen, S.K., Boschung, J., Nauels, A., Xia, Y., Bex, V., Midgley, P.M. (Eds.), 2013. Climate Change 2013: The Physical Science Basis. Contribution of Working Group I to the Fifth Assessment Report of the Intergovernmental Panel on Climate Change. Cambridge University Press, Cambridge, United Kingdom and New York, NY, USA.

Takahashi, T., Broecker, W.S., Langer, S., 1985. Redfield ratio based on chemical data from isopycnal surfaces. J. Geophys. Res. 90, 6907–6924. doi:10.1029/JC090iC04p06907.

Takahashi, T., Sutherland, S.C., Wanninkhof, R., Sweeney, C., Feely, R.A., Chipman, D.W., Hales, B., Friederich, G., Chavez, F., Sabine, C., 2009. Climatological mean and decadal change in surface ocean pCO_2 and net sea–air CO_2 flux over the global oceans. Deep Sea Res. Part II Top. Stud. Oceanogr. 56, 554–577.

Tanhua, T., Biastoch, A., Körtzinger, A., Lüger, H., Böning, C., Wallace, D.W.R., 2006. Changes of anthropogenic CO2 and CFCs in the North Atlantic between 1981 and 2004. Glob. Biogeochem. Cycles 20, 13 PP. doi:200610.1029/2006GB002695

Tomczak, M., 1981. A multi-parameter extension of temperature/salinity diagram techniques for the analysis of non-isopycnal mixing. Prog. Oceanogr. 10, 147–171.

van Aken, H.M., 2000. The hydrography of the mid-latitude Northeast Atlantic Ocean: II: The intermediate water masses. Deep Sea Res. Part Oceanogr. Res. Pap. 47, 789–824. doi:10.1016/S0967-0637(99)00112-0.

Vázquez-Rodríguez, M., Touratier, F., Lo Monaco, C., Waugh, D.W., Padín, X.A., Bellerby, R.G.J., Goyet, C., Metzl, N., Ríos, A.F., Pérez, F.F., 2009a. Anthropogenic carbon distributions in the Atlantic Ocean: data-based estimates from the Arctic to the Antarctic. Biogeosciences 6, 439–451.

Vázquez-Rodríguez, M., Padín, X.A., Ríos, A.F., Bellerby, R.G.J., Pérez, F.F., 2009b. An upgraded carbon-based method to estimate the anthropogenic fraction of dissolved CO_2 in the Atlantic Ocean. Biogeosciences Discussions 6, 4527–4571. http://dx.doi.org/10.1016/j.jmarsys.2011.11.023.

Vázquez-Rodríguez, M., Padín, X.A., Pardo, P.C., Ríos, A.F., Pérez, F.F., 2012. The subsurface layer reference to calculate preformed alkalinity and air–sea CO_2 disequilibrium in the Atlantic Ocean. J. Mar. Syst. 94, 52–63. doi:10.1016/j.jmarsys.2011.10.008.

Velo, A., Vázquez-Rodríguez, M., Padín, X.A., Gilcoto, M., Ríos, A.F., Pérez, F.F., 2010. A multiparametric method of interpolation using WOA05 applied to anthropogenic CO2 in the Atlantic. Sci. Mar. 74, 21–32.

Watson, A.J., Schuster, U., Bakker, D.C.E., Bates, N.R., Corbiere, A., Gonzalez-Davila, M., Friedrich, T., Hauck, J., Heinze, C., Johannessen, T., Kortzinger, A., Metzl, N., Olafsson, J., Olsen, A., Oschlies, A., Padin, X.A., Pfeil, B., Santana-Casiano, J.M., Steinhoff, T., Telszewski, M., Rios, A.F., Wallace, D.W.R., Wanninkhof, R., 2009. Tracking the Variable North Atlantic Sink for Atmospheric CO_2. Science 326, 1391–1393. doi:10.1126/science.1177394.

Woosley, R. J., Millero, F. J., Wanninkhof, R., 2016. Rapid anthropogenic changes in CO2 and Ph in the Atlantic Ocean: 2003–2014. Global Biogeochem. Cycles, 30. doi:10.1002/2015GB005248.

Zunino, P., Garcia-Ibañez, M.I., Lherminier, P., Mercier, H., Rios, A.F., Pérez, F.F., 2014. Variability of the transport of anthropogenic CO_2 at the Greenland–Portugal OVIDE section: controlling mechanisms. Biogeosciences 11, 2375–2389. doi:10.5194/bg-11-2375-2014.